

Unveiling Damage Mechanisms of Chromium-coated Zirconium-based Fuel Claddings

A Thesis

Presented to

the faculty of the School of Engineering and Applied Science

University of Virginia

in partial fulfillment
of the requirements for the degree

Master of Science

by

Alex I Jarama

May 2020

Dedication

To my buddy, Max.

Acknowledgements

I would like to first thank my family and friends for their support during my graduate career.

I wish to thank Westinghouse Electrical Company for providing the coated cladding material used in this work. I am extraordinary grateful to Jorie Walters and Benjamin Maier from Westinghouse for providing me with critical insight and feedback on the work presented in this thesis.

I thank my advisor, Dr. Xiaodong (Chris) Li, for his mentorship and support during my time as a graduate student.

I would also like to thank several of my lab mates for their support with the work presented in this thesis. Specifically, I thank Morgan Price for her support with high temperature testing and data processing. I thank David Roache for his support with mechanical, data processing, and SEM imaging. I thank Frederick Michael Heim for his support with mechanical testing, data processing, and SEM imaging. Lastly, I would like to thank Clifton Bumgardner for his support with mechanical testing, data processing and SEM imaging, in addition to serving as a mentor during my time in graduate school. I am grateful to have had the opportunity to work with them and the rest of my lab mates these past few years.

The material presented here is based upon work supported by the Department of Energy under Award Numbers DE-NE0008222 and DE-NE0008824. This report was prepared as an account of work sponsored by an agency of the United States Government. Neither the United States Government nor any agency thereof, nor any of their employees, makes any warranty, express or implied, or assumes any legal liability or responsibility for the accuracy, completeness, or usefulness of any information, apparatus, product, or process disclosed, or represents that its use would not infringe privately owned rights. Reference herein to any specific commercial product, process, or service by trade name, trademark, manufacturer, or otherwise does not necessarily constitute or imply its endorsement, recommendation, or favoring by the United States Government or any agency thereof. The views and opinions of authors expressed herein do not necessarily state or reflect those of the United States Government or any agency thereof.

Abstract

Coated nuclear fuel claddings offer a promising, near-term solution to address the demand for next-generation, accident-tolerant fuel systems and possess superior mechanical properties and greater oxidation resistance compared to current cladding technology, allowing for improved performance during beyond design-basis accident conditions. Here, we unveil the room temperature (23 °C) and high temperature (315 °C) failure mechanisms of chromium-coated zirconium alloys using a novel mechanical test rig coupled with in-situ three-dimensional digital image correlation and acoustic emissions sensing to monitor spatial strain and crack initiation / propagation during cladding expansion. Ex-situ scanning electron microscopy was used to characterize crack propagation at various levels of strain and temperature. Axial cracking along the full circumference of the room temperature samples was observed, while angled cracks along the surface were observed in the high temperature samples. Through-thickness cracking was observed in both room temperature and high temperature samples. The differing fracture mechanisms observed between room temperature and high temperature samples will carry significant implications for their use in reactor environments.

Table of Contents

Dedication.....	1
Acknowledgements.....	2
Abstract.....	3
Table of Contents.....	4
List of Figures.....	6
Nomenclature.....	8
Chapter 1: Introduction.....	9
Section 1.1: Background on Nuclear Reactors.....	11
Section 1.2: Background on Zirconium Alloys.....	13
Section 1.3: Prior Work on Chromium-coated Zirconium-based Fuel Claddings.....	14
Section 1.4: Scope of Thesis.....	16
References.....	18
Chapter 2: Overview of Digital Image Correlation, Acoustic Emission, Expanding Plug Testing, and 4-point Bending Testing.....	24
Section 2.1: Digital Image Correlation Overview.....	24
Section 2.2: Acoustic Emissions to Detect Cracks.....	28
Section 2.3: Expanding Plug Mechanical Testing.....	29
Section 2.4: Four-point Bending Mechanical Testing.....	31
Section 2.5: Summary.....	32
References.....	33
Chapter 3: Overview of Room Temperature (23 °C) and High Temperature Testing (315 °C) Methodologies.....	35
Section 3.1: Material Preparation.....	35
Section 3.2: Data Capturing.....	36
Section 3.3: Room Temperature Mechanical Testing.....	37
Subsection 3.3.1: Expanding Plug.....	37
Subsection 3.3.2: Four-point Bending.....	38
Section 3.4: High Temperature Mechanical Testing.....	38
Section 3.5: Crack Characterization.....	40
Section 3.6: Acoustic Emission Data Processing.....	41
Section 3.7: Digital Image Correlation Data Processing.....	42
References.....	47
Chapter 4: Failure Mechanisms at Room Temperature (23 °C).....	50
Section 4.1: Room Temperature Mechanical Testing.....	51
Subsection 4.1.1 Expanding Plug.....	51

Subsection 4.1.2 Four-point Bending.....	54
Section 4.2: Room Temperature Crack Characterization.....	57
Subsection 4.2.1 Expanding Plug.....	57
Subsection 4.2.2 Four-point Bending.....	60
Section 4.3: Summary.....	62
References.....	64
Chapter 5: Failure Mechanisms at High Temperature (315 °C).....	65
Section 5.1: High Temperature Expanding Plug Testing.....	65
Section 5.2: High Temperature Crack Characterization.....	69
Section 5.3: Summary.....	71
References.....	73
Chapter 6: Conclusions and Future Work.....	74
References.....	78

List of Figures

Figure 1.1:	Overview of a Nuclear Fuel Assembly.....	12
Figure 1.2:	Cross-sectional SEM Observation of Cr-coated Zircaloy-4 Cladding Tubes After Ring Tensile Tests at 2, 4, and 6 % Strain.....	15
Figure 2.1:	Schematic of a Typical 3D-DIC Setup.....	24
Figure 2.2:	Illustration of 3D-DIC Displacement Vector between Undeformed and Deformed Subsets.....	27
Figure 2.3:	3D-DIC Intrinsic Errors Can Be Categorized into Image Correlation and Calibration Errors; Listed Are Some Factors That Affect Each Type of Error....	28
Figure 2.4:	Definitions of Acoustic Event Parameters.....	29
Figure 2.5:	Expanding Plug Test Setup.....	30
Figure 2.6:	Four-point Bending Test Setup.....	31
Figure 3.1:	Schematic of a Typical (a) Expanding Plug and (b) Four-point Bend Test Setup.....	39
Figure 3.2:	Schematic of a High Temperature Expanding Plug Test Setup.....	40
Figure 3.3:	Example Camera-to-sample Angle Plot, Showing Convergence of Data.....	44
Figure 3.4:	Effect of Image Averaging on (a) Hoop Stress vs. Hoop Strain Curve and (b) Hoop Strain Error.....	45
Figure 4.1:	σ_{hoop} vs. ϵ_{hoop} for (a) E and (c) ES specimens and Normalized Cumulative Acoustic Energy vs. ϵ_{hoop} for (b) E and (d) ES specimens.....	53
Figure 4.2:	Typical Spatial ϵ_{hoop} Progression During an Expanding Plug Test, Here for ES04, at (a) First AE Event, (b) First Significant AE Event, (c) Second Cluster of AE Events, and (d) at Test Endpoint.....	54
Figure 4.3:	(a) σ_{xx} vs. ϵ_{xx} and (b) Normalized Cumulative Acoustic Energy vs. ϵ_{xx}	55
Figure 4.4:	Typical Spatial Strain Progression During a Four-point Bend Test, Here for B03, at (a) 0.2% ϵ_{xx} , (b) First Significant AE Event, (c) Crack Opening during AE Cluster, and (d) at Test Endpoint.....	56
Figure 4.5:	Representative SEM Images at the Surface (Left) and Cross-section (right) for Expanding Plug Specimens: (a) Schematic of the Loading/Cracking Conditions	

and the Specimen Orientation, (b-e) Cracking at Increasing Levels of ϵ_{hoop}58

Figure 4.6: Representative SEM Images for Bending Specimen B03: (a) a Schematic of the Loading/Cracking Conditions and the Sample Orientation for SEM Imaging, (b) Several Visible Grinding Marks, (c) Thin Cracking in the Transverse Direction, and (d) Opening of the Striations.....61

Figure 5.1: a) σ_{hoop} vs. ϵ_{hoop} for HE Specimens and b) Normalized Cumulative Acoustic Energy vs. ϵ_{hoop} for HE Specimens.....67

Figure 5.2: Typical Spatial ϵ_{hoop} Progression during an Expanding Plug Test, Here for HE03.....69

Figure 5.3: SEM Images of HE05: (a) Image of Specimen Surface in Region of Greatest Deformation Showing Angled Cracks, (b) Image of Specimen Cross-Section Showing Through-thickness Cracking.....70

Nomenclature:

3D-DIC:	Three-dimensional Digital Image Correlation
AE:	Acoustic Emission
ATF:	Accident Tolerant Fuel
BDBA:	Beyond Design-Basis Solutions
CCD:	Charge-coupled Device
CTE:	Coefficient of Thermal Expansion
DIC:	Digital Image Correlation
LWR:	Light Water Reactor
NDT:	Nondestructive Detection Technique
PWR:	Pressurized Water Reactor
SEM:	Scanning Electron Microscopy

Chapter 1: Introduction

The Fukushima Daiichi nuclear disaster in Japan on March 11, 2011 was the most severe nuclear accident since the 1986 Chernobyl disaster in Ukraine. The 9.0 magnitude earthquake off the eastern coast of Japan triggered powerful tsunamis throughout the region, and all four nuclear power plants in Japan were shut down, as a result [1]. Although it is standard procedure to shut down a nuclear plant following any signs of seismic activity, heat is still generated by the radioactive decay of fission products [2,3]. In order to prevent a nuclear meltdown and the release of radiation into the immediate environment, the nuclear reactor needs to be continuously cooled for at least a day [1,4]. Backup diesel generators located underground powered the cooling of the nuclear reactor immediately after the earthquake hit, but the high waves from the tsunami soon flooded the plant and rendered the generators inoperable [1,4]. With no electricity to transmit coolant to the reactors, the elevated temperatures not only caused nuclear fuel to melt and escape into the surrounding environment, but also caused oxidation of the zirconium fuel cladding [1,5,6]. This oxidation led to the production of hydrogen, which soon leaked into adjacent buildings and caused explosions, severely damaging major equipment and the piping systems of the nuclear plant and releasing further radiation to the immediate area [5,6].

The devastating impacts of the earthquake and tsunami are still felt today. Almost 20,000 people lost their lives, while more than 400,000 people were forced to evacuate at the time [1,7]. More than 130,000 buildings were destroyed, and over \$360 billion in economic losses were incurred, making the earthquake one of the most expensive disasters in history [1,7]. Although no deaths were directly attributed to the nuclear disaster, the Japanese government drew sharp criticism for its handling of and response to the nuclear meltdown [7]. Prior to this disaster, a number of countries, such as Germany and Italy, planned on scaling up their nuclear energy

operations, in order to offset their dependence on fossil fuels and reduce carbon dioxide emissions [8,9]. The Fukushima nuclear disaster quickly altered public opinion on nuclear energy, and some countries, including Germany and Italy, subsequently announced plans to stop all nuclear operations [8,9].

Nine years after the disaster, nuclear energy has started to make a resurgence in a number of countries, despite lingering negative public opinion. In the years immediately following Fukushima, many of Japan's nuclear plants were shut down, and Japan's reliance on nuclear energy plummeted from 30% to 5% [10]. In order to comply with its energy demands, Japan expanded its use of fossil fuels, and in 2018 fossil fuels comprised 85% of Japan's entire energy production [11]. Due to the global need of curbing carbon emissions, the Japanese government decided to restart its nuclear energy program in 2015, seeking to have nuclear energy make up 20% of its energy supply by 2030 [12]. Despite taking a major hit in production after Fukushima, the global nuclear energy industry recovered and reached pre-Fukushima levels in 2018, with nuclear energy supplying almost 10% of the energy demand worldwide [13,14]. In 2018 the United States had 96 operating nuclear reactors, and more than 50 nuclear reactors were under construction worldwide [15].

In 2017, fossil fuels generated 64.5% of all electricity worldwide, while nuclear energy met only 10% of the global energy demand [16,17]. The United States Energy Information Administration projects global energy consumption to grow by nearly 50% between 2018 and 2050 [18]. In order to address the growing global energy demand and the immediate issue of climate change today, carbon neutral energy sources, including nuclear energy, need to comprise a larger share of the electric grid worldwide. Although nuclear disasters, such as Fukushima, have increased negative public opinion surrounding nuclear reactors, nuclear energy is a proven

technology, that must be a component of the comprehensive global response to climate change alongside renewable energy technology.

Unlike fossil fuels, nuclear reactors do not directly produce carbon dioxide and have a much higher fuel to power output ratio than other energy sources, including fossil fuels [14,15]. Although upfront costs to build a nuclear plant can range between \$5 and \$10 billion, the electricity generated from nuclear reactors is cheaper than fossil fuel plants [15,19]. Despite common public opinion, nuclear energy is considered a safer energy source than fossil fuels [20]. According to a 2016 study, both nuclear and renewable energy sources have death rates hundreds of times lower than fossil fuel sources per terawatt-hour of energy production [20]. Part of the work that needs to be done in the immediate future is reducing the stigma surrounding nuclear energy. One way to do that is improving the reliability and durability of different components in a nuclear reactor, especially during loss-of-coolant accident conditions, such as Fukushima. This thesis specifically presents a testing methodology to characterize and understand the key damage mechanisms of coated nuclear fuel claddings at room temperature and operating temperature for a light water nuclear reactor.

1.1 Background on Nuclear Reactors

Nuclear reactors are the site of nuclear fission, a process that releases a tremendous amount of energy (heat) when the nucleus of an atom splits into two or more smaller nuclei, known as fission products [21,22]. Uranium is used to power the fission process, and it is processed down to manufacture ceramic nuclear fuel pellets [21,23]. As Figure 1.1 illustrates, these pellets are typically only 1 cm in diameter, and they are stacked inside 4 m metal tubes called fuel cladding [21,24,25]. These tubes are sealed on both ends to form a fuel rod [24]. In a typical fuel assembly between 100 and 300 fuel rods are bundled together in a square pattern before being installed in

the reactor core [24,25]. Most nuclear reactors today have several hundred fuel assemblies immersed in water, each containing thousands of nuclear fuel pellets to power nuclear fission [26].

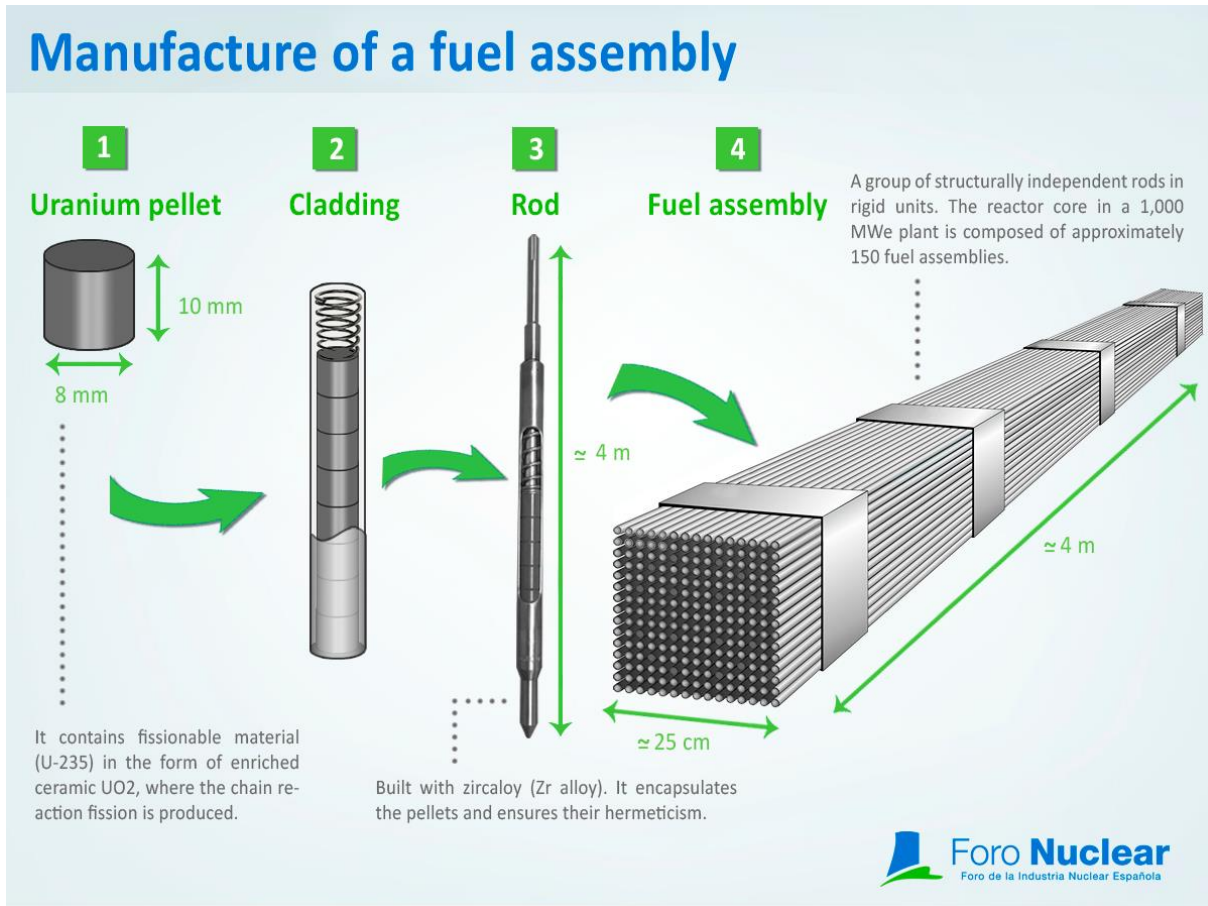


Figure 1.1: Overview of a Nuclear Fuel Assembly. [25]

In the United States all commercial nuclear reactors are light-water reactors (LWRs) [21]. The two types of LWRs include boiling water reactors and pressurized water reactors (PWRs), both of which use water as a coolant and neutron moderator to control nuclear fission [21]. PWRs are the main type of LWR used, and these reactors pump water into the reactor core, which operates at temperatures above 300°C [21,27,28]. The intense pressure in a PWR prevents the water from boiling at 100°C when running through the reactor core [21]. The heated water then is run through tubes inside a heat exchanger, where an external water source is then heated to create steam [21]. Similar to coal powered plants, the steam is used to drive turbines to produce electricity [21,26].

Generally, nuclear plants are capable of running for several months and even years without interruption, thus supplying constant power when in use [26].

1.2 Background on Zirconium Alloys

The recent emphasis on accident tolerant fuel (ATF) in the nuclear energy industry has manifested itself into the development of improved reactor components with a major focus on fuel claddings [29,30]. Fuel claddings for light water reactors (LWRs) have traditionally been comprised of zirconium alloys (Zr-alloys), which perform excellently under nominal operating conditions due to their low neutron absorption, corrosion resistance, and ability to operate at high temperatures [31]. However, a desire to improve the fuel cladding oxidation resistance in high temperature water and steam during accident conditions has directed research towards beyond design-basis accident (BDBA) solutions [32-34]. Particularly, sustained operation at elevated temperatures, especially above 1200 °C, has come under focus, since such an extreme environment can lead to rapid oxidation of the zirconium cladding, mechanical degradation, and catastrophic failure [35,36].

Several types of coatings, ranging from iron chromium aluminum alloy [37-40] to titanium nitride [41-43] to chromium coatings [39,40,44-28], are being investigated to enhance the mechanical performance of existing Zr-alloy fuel claddings. Since the application of a thin coating has relatively minor implications on the current manufacturing process, this particular solution has emerged as one of leading alternatives for next-generation claddings. In this study, chromium-coated claddings are considered due to their superlative high temperature mechanical properties [44,49,50] and corrosion resistance [51–53]. Before coated Zr-alloy claddings are reliability integrated into nuclear reactors, it is first necessary to investigate the underlying mechanisms that lead to coating failure, such as cracking, in order to improve the performance of the claddings.

The author notes that the majority of Section 1.2 is adapted from the author's peer reviewed journal article titled "Unveiling Damage Mechanisms of Chromium-Coated Zirconium-Based Fuel Claddings by Coupling Digital Image Correlation and Acoustic Emission" published in *Materials Science and Engineering: A* [54].

1.3 Prior Work on Chromium-coated Zirconium-based Fuel Claddings

The fuel cladding is the separator between nuclear fuel and coolant in nuclear reactors [55]. The fuel cladding is the first part to break during loss-of-coolant accident conditions, and therefore, it is fundamentally important to fully understand the fracture mechanisms of coated claddings [55]. This thesis specifically addresses the fracture mechanisms of chromium-coated zirconium-based fuel claddings.

In 2015 a research group in the Republic of Korea published a study on the adhesion and high temperature oxidation behavior of chromium-coated Zircaloy-4 cladding tubes [56]. Ring tensile tests up to 2, 4, and 6 % strain were conducted, and cross-sectional images of representative samples from each test are illustrated in Figure 1.2 [56]. No through-thickness cracking was observed in samples loaded to 2 and 4 % strain, thus indicating that the onset of cracking can be correlated to strains between 4 and 6 % [56]. It should be noted that the chromium coating in these samples was applied using a 3D laser coating process [56], which differs from the cold-spray process used to apply the coating in the samples examined in this thesis. This work thus offers a point of comparison to determine if the cracking behavior of coated fuel claddings differs due to loading mode and the coating application process used at room temperature. The steam oxidation studies conducted by this group at 1200 °C showed that the chromium coating helped to greatly slow down the formation of an oxide layer, showcasing the effectiveness of chromium coatings to prevent oxidation of the zirconium-based fuel cladding [56]. Although high temperature oxidation

of fuel claddings is not considered in this thesis specifically, oxidation of the underlying zirconium-based fuel cladding is of utmost concern to the nuclear energy community, because oxidation of the cladding in a loss-of-coolant accident can lead to a hydrogen explosion [56]. In the pursuit to assess the effectiveness of coated claddings against oxidation, the failure mechanisms below 1200 C (beyond design-basis accident conditions) need to be also considered, in order to determine when oxidation of the fuel cladding compromises the integrity of the entire system.

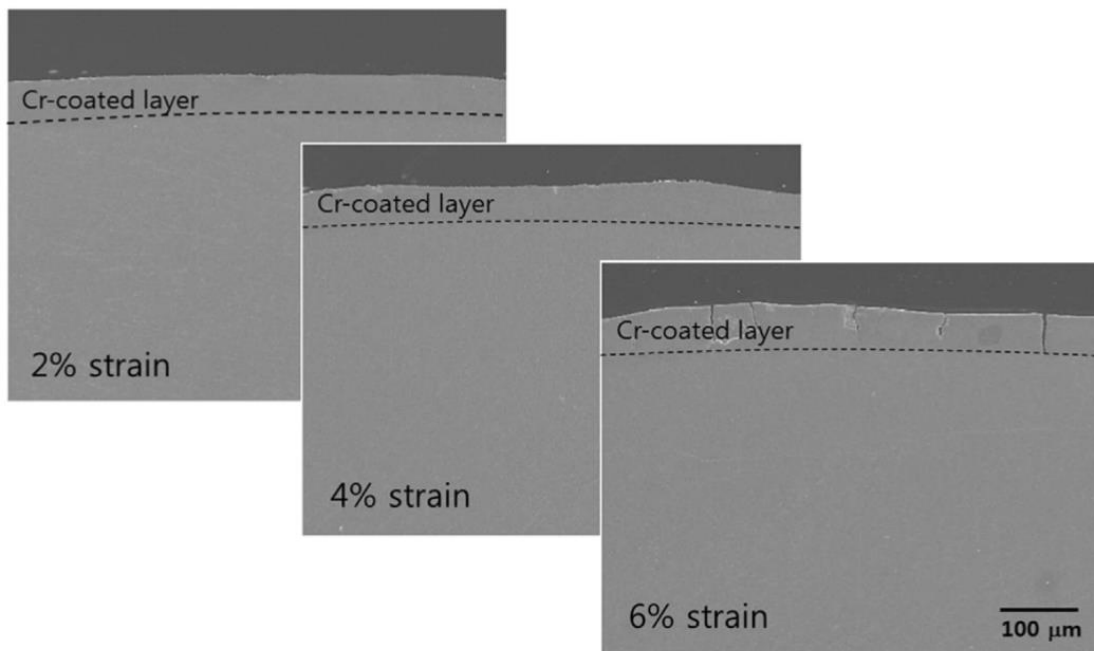


Figure 1.2: Cross-sectional SEM Observation of Cr-coated Zircaloy-4 Cladding Tubes After Ring Tensile Tests at 2, 4, and 6 % Strain. [56]

Although, it is evident from examining the literature that a number of important studies have been conducted examining corrosion, fretting, and oxidation resistance of chromium-coated fuel claddings [57-59], the author finds that there is a lack of studies examining the cracking behavior of these coated claddings at room temperature and at elevated temperatures, besides 1200 °C [60]. Even though studies, such as [56], correlate strain ranges to cracking behavior,

critical strain thresholds have not been correlated to key cracking behaviors, such as the onset of cracking. As described in this work, DIC and AE techniques are coupled to correlate spatial measurements to key coating cracking events, allowing for evaluation of the coating's integrity during deformation. The unprecedented work described here not only examines the cracking behavior of coated cladding material at room temperature, but also examines that same behavior at the operating temperature of a nuclear reactor (315 °C). The work presented here provides a unique testing methodology to gain a fundamental understanding of the key mechanisms behind coating cracking. This methodology can be used to evaluate the integrity of other coated claddings to further investigate the role different parameters, such as coating application process, coating thickness, and temperature, play in terms of integrity of the coating. Although not all these parameters are considered in this work, the insights presented here provide a good start to filling the knowledge gap of linking deformation to cracking behavior in coated nuclear fuel rods.

1.4 Scope of Thesis

In this work, the fracture mechanisms of chromium-coated Zr-alloy claddings via digital image correlation and acoustic emissions mechanical testing at room temperature (23°C) and at 315°C, the typical operating temperature for a nuclear reactor, are investigated. These *in situ* measurement techniques are paired with mechanical testing to correlate deformation with key cracking behavior. Primary attention was given to the expanding plug methodology to evaluate cracking under cladding expansion, which poses the greatest threat to fuel claddings. This thesis contains six chapters. Chapter 2 provides a brief overview on the digital image correlation (DIC) and acoustic emission (AE) techniques, in addition to expanding plug and four-point bending mechanical testing. Chapter 3 presents the testing methodology for fuel cladding testing at room

temperature and at nuclear reactor operating temperature. Chapter 4 presents the results and a discussion of the room temperature experiments, and Chapter 5 presents the results and initial observations made for the operating temperature experiments. Lastly, Chapter 6 provides a brief synopsis of all the key findings of this thesis and provides recommendations for future testing.

References

- [1] S. Yeo, “Analysis: The legacy of the Fukushima nuclear disaster,” *Carbon Brief*, 10-Mar-2016. [Online]. Available: <https://www.carbonbrief.org/analysis-the-legacy-of-the-fukushima-nuclear-disaster>.
- [2] “Decay Heat - Decay Energy,” *Nuclear Power*. [Online]. Available: <https://www.nuclear-power.net/nuclear-power/reactor-physics/reactor-operation/residual-heat/decay-heat-decay-energy/>.
- [3] “Earthquakes and Nuclear Power Plants,” *Science On a Sphere*. [Online]. Available: <https://sos.noaa.gov/datasets/earthquakes-and-nuclear-power-plants/>.
- [4] M. Nutt, “Spent Fuel.” [Online]. Available: https://www.ne.anl.gov/pdfs/nuclear/spent_fuel_nutt.pdf.
- [5] E. Hollnagel and Y. Fujita, “The Fukushima Disaster – Systemic Failures as The Lack of Resilience,” *Nuclear Engineering and Technology*, 02-Apr-2015. [Online]. Available: <https://www.sciencedirect.com/science/article/pii/S1738573315300024>.
- [6] A. Abe, C. Giovedi, D. D. S. Gomes, and A. T. E. Silva, “Revisiting Stainless Steel as PWR Fuel Rod Cladding after Fukushima Daiichi Accident,” *Journal of Energy and Power Engineering*, vol. 8, no. 6, Jun. 2014.
- [7] E. Ferris and M. Solís, “Earthquake, Tsunami, Meltdown – The Triple Disaster's Impact on Japan, Impact on the World,” *Brookings*, 29-Jul-2016. [Online]. Available: <https://www.brookings.edu/blog/up-front/2013/03/11/earthquake-tsunami-meltdown-the-triple-disasters-impact-on-japan-impact-on-the-world/>.
- [8] R. Staudenmaier, “Germany's nuclear phase-out explained: DW: 15.06.2017,” 15-Jun-2017. [Online]. Available: <https://www.dw.com/en/germanys-nuclear-phase-out-explained/a-39171204>.
- [9] “Nuclear Power in the World Today.” [Online]. Available: <https://www.world-nuclear.org/information-library/current-and-future-generation/nuclear-power-in-the-world-today.aspx>.
- [10] K. Olsen, “No to nuclear: Japan wants reactors phased out, post-Fukushima,” 19-Dec-2019. [Online]. Available: <https://www.aljazeera.com/news/2019/12/japanese-turn-nuclear-decade-wrought-fukushima-191220000003532.html>.
- [11] J. Conca, “Shutting Down All Of Japan's Nuclear Plants After Fukushima Was A Bad Idea,” 31-Oct-2019. [Online]. Available: <https://www.forbes.com/sites/jamesconca/2019/10/31/shutting-down-japans-nuclear-plants-after-fukushima-was-a-bad-idea/#794ee5bf19a4>.

- [12] “Nuclear Power in Japan.” [Online]. Available: <https://www.world-nuclear.org/information-library/country-profiles/countries-g-n/japan-nuclear-power.aspx>.
- [13] “Global energy demand rose by 2.3% in 2018, its fastest pace in the last decade - News,” 26-Mar-2019. [Online]. Available: <https://www.iea.org/news/global-energy-demand-rose-by-23-in-2018-its-fastest-pace-in-the-last-decade>.
- [14] K. Rooney, “This is what nuclear power looks like 8 years after Fukushima,” World Economic Forum, 11-Dec-2019. [Online]. Available: <https://www.weforum.org/agenda/2019/12/japan-nuclear-power-reactor-fukushima/>.
- [15] “Nuclear Energy Pros & Cons,” Renewable Resources Coalition, 19-Nov-2019. [Online]. Available: <https://www.renewableresourcescoalition.org/nuclear-energy-pros-cons/>.
- [16] “Where does our electricity come from?” [Online]. Available: <https://www.world-nuclear.org/nuclear-essentials/where-does-our-electricity-come-from.aspx>.
- [17] V. Petrova, “Renewables supply 25% of global power in 2017 - IEA,” 22-Mar-2018. [Online]. Available: <https://renewablesnow.com/news/renewables-supply-25-of-global-power-in-2017-iea-606070/>.
- [18] “EIA projects nearly 50% increase in world energy usage by 2050, led by growth in Asia,” Today in Energy, 24-Sep-2019. [Online]. Available: <https://www.eia.gov/todayinenergy/detail.php?id=41433>.
- [19] B. Plumer, “Why America abandoned nuclear power (and what we can learn from South Korea),” 29-Feb-2016. [Online]. Available: <https://www.vox.com/2016/2/29/11132930/nuclear-power-costs-us-france-korea>.
- [20] H. Ritchie, “What are the safest sources of energy?,” 10-Feb-2020. [Online]. Available: <https://ourworldindata.org/safest-sources-of-energy>.
- [21] “NUCLEAR 101: How Does a Nuclear Reactor Work?,” 06-Feb-2019. [Online]. Available: <https://www.energy.gov/ne/articles/nuclear-101-how-does-nuclear-reactor-work>.
- [22] “Fission products.” [Online]. Available: https://www.radioactivity.eu.com/site/pages/Fission_Products.htm.
- [23] “Nuclear fuel pellets,” 11-Oct-2015. [Online]. Available: https://www.our-energy.com/nuclear_fuel_pellets.html.
- [24] “What is Nuclear Fuel?,” United States Nuclear Regulatory Commission - Protecting People and the Environment, 19-Oct-2018. [Online]. Available: <https://www.nrc.gov/reading-rm/basic-ref/students/science-101/what-is-an-nuclear-fuel.html>.

- [25] “Manufacture of a fuel assembly,” Foro Nuclear, 18-Oct-2018. [Online]. Available: <https://www.foronuclear.org/en/press-room/infographics/124274-manufacture-of-a-fuel-assembly>.
- [26] “How does a nuclear reactor work - World Nuclear Association.” [Online]. Available: <https://www.world-nuclear.org/nuclear-essentials/how-does-a-nuclear-reactor-work.aspx>.
- [27] “LWR - Light Water Reactor.” [Online]. Available: <https://www.nuclear-power.net/nuclear-power-plant/reactor-types/lwr-light-water-reactor/>.
- [28] “Nuclear Power Reactors,” World Nuclear Association. [Online]. Available: <https://www.world-nuclear.org/information-library/nuclear-fuel-cycle/nuclear-power-reactors/nuclear-power-reactors.aspx>.
- [29] K. Barrett, S. Bragg-Sitton, and D. Galicki, “Advanced LWR Nuclear Fuel Cladding System Development Trade-off Study,” Sep-2012. [Online]. Available: https://www.energy.gov/sites/prod/files/M3LW-12IN0502028_Tradeoff_study_report.pdf.
- [30] Z. Duan, H. Yang, Y. Satoh, K. Murakami, S. Kano, Z. Zhao, J. Shen, and H. Abe, “Current status of materials development of nuclear fuel cladding tubes for light water reactors,” *Nuclear Engineering and Design*, vol. 316, pp. 131–150, May 2017.
- [31] K. Barrett, S. Bragg-Sitton, and D. Galicki, “Advanced LWR Nuclear Fuel Cladding System Development Trade-off Study,” Sep-2012. [Online]. Available: https://www.energy.gov/sites/prod/files/M3LW-12IN0502028_Tradeoff_study_report.pdf.
- [32] M. Moalem and D. Olander, “Oxidation of Zircaloy by steam,” *Journal of Nuclear Materials*, vol. 182, pp. 170–194, 1991.
- [33] S. Zinkle and G. Was, “Materials challenges in nuclear energy,” *Acta Materialia*, vol. 61, no. 3, pp. 735–758, Feb. 2013.
- [34] A. T. Motta, A. Couet, and R. J. Comstock, “Corrosion of Zirconium Alloys Used for Nuclear Fuel Cladding,” *Annual Reviews*, Apr-2015. [Online]. Available: <https://www.annualreviews.org/doi/10.1146/annurev-matsci-070214-020951>.
- [35] Z. Karoutas, J. Brown, A. Atwood, L. Hallstadius, E. Lahoda, S. Ray, and J. Bradfute, “The maturing of nuclear fuel: Past to Accident Tolerant Fuel,” *Progress in Nuclear Energy*, vol. 102, pp. 68–78, Jan. 2018.
- [36] C. Duriez, D. Drouan, and G. Pouzadoux, “Reaction in air and in nitrogen of pre-oxidised Zircaloy-4 and M5™ claddings,” *Journal of Nuclear Materials*, vol. 441, no. 1-3, pp. 84–95, Oct. 2013.
- [37] K. A. Terrani, C. M. Parish, D. Shin, and B. A. Pint, “Protection of zirconium by alumina- and chromia-forming iron alloys under high-temperature steam exposure,” *Journal of*

- Nuclear Materials, vol. 438, no. 1-3, pp. 64–71, Jul. 2013.
- [38] J. K. Bunn, R. L. Fang, M. R. Albing, A. Mehta, M. J. Kramer, M. F. Besser, and J. R. Hattrick-Simpers, “A high-throughput investigation of Fe–Cr–Al as a novel high-temperature coating for nuclear cladding materials,” *Nanotechnology*, vol. 26, no. 27, p. 274003, Jun. 2015.
- [39] B. Maier, H. Yeom, G. Johnson, T. Dabney, J. Walters, J. Romero, H. Shah, P. Xu, and K. Sridharan, “Development of Cold Spray Coatings for Accident-Tolerant Fuel Cladding in Light Water Reactors,” *Jom*, vol. 70, no. 2, pp. 198–202, Nov. 2017.
- [40] J.H. Park, H.-G. Kim, J.-Y. Park, Y.-I. Jung, D.-J. Park, and Y.-H. Koo, “High temperature steam-oxidation behavior of arc ion plated Cr coatings for accident tolerant fuel claddings,” *Surface and Coatings Technology*, vol. 280, pp. 256–259, Oct. 2015.
- [41] E. Alat, A. T. Motta, R. J. Comstock, J. M. Partezana, and D. E. Wolfe, “Multilayer (TiN, TiAlN) ceramic coatings for nuclear fuel cladding,” *Journal of Nuclear Materials*, vol. 478, pp. 236–244, Sep. 2016.
- [42] F. Khatkhatay, L. Jiao, J. Jian, W. Zhang, Z. Jiao, J. Gan, H. Zhang, X. Zhang, and H. Wang, “Superior corrosion resistance properties of TiN-based coatings on Zircaloy tubes in supercritical water,” *Journal of Nuclear Materials*, vol. 451, no. 1-3, pp. 346–351, Aug. 2014.
- [43] I. Kim, F. Khatkhatay, L. Jiao, G. Swadener, J. I. Cole, J. Gan, and H. Wang, “TiN-based coatings on fuel cladding tubes for advanced nuclear reactors,” *Journal of Nuclear Materials*, vol. 429, no. 1-3, pp. 143–148, Oct. 2012.
- [44] A. Kuprin, V. Belous, V. Voyevodin, V. Bryk, R. Vasilenko, V. Ovcharenko, E. Reshetnyak, G. Tolmachova, and P. Vyugov, “Vacuum-arc chromium-based coatings for protection of zirconium alloys from the high-temperature oxidation in air,” *Journal of Nuclear Materials*, vol. 465, pp. 400–406, Oct. 2015.
- [45] J.-C. Brachet, M. Le Saux, M. Flem, and S. Urvoy, “On-Going Studies at CEA On Chromium Coated Zirconium Based Nuclear Fuel Claddings for Enhanced Accident Tolerant LWRs Fuel,” Sep-2015. [Online]. Available: https://www.researchgate.net/publication/283446965_On-Going_Studies_At_Cea_On_Chromium_Coated_Zirconium_Based_Nuclear_Fuel_Claddings_For_Enhanced_Accident_Tolerant_Lwrs_Fuel.
- [46] H.G. Kim, I.-H. Kim, Y.-I. Jung, D.-J. Park, J.-Y. Park, and Y.-H. Koo, “Adhesion property and high-temperature oxidation behavior of Cr-coated Zircaloy-4 cladding tube prepared by 3D laser coating,” *Journal of Nuclear Materials*, vol. 465, pp. 531–539, Oct. 2015.
- [47] M. Ševeček, A. Gurgen, A. Seshadri, Y. Che, M. Wagih, B. Phillips, V. Champagne, and

- K. Shirvan, "Development of Cr cold spray-coated fuel cladding with enhanced accident tolerance," *Nuclear Engineering and Technology*, vol. 50, no. 2, pp. 229–236, Mar. 2018.
- [48] B. Maier, H. Yeom, G. Johnson, T. Dabney, J. Walters, P. Xu, J. Romero, H. Shah, and K. Sridharan, "Development of cold spray chromium coatings for improved accident tolerant zirconium-alloy cladding," *Journal of Nuclear Materials*, vol. 519, pp. 247–254, Jun. 2019.
- [49] U. Holzwarth and H. Stamm, "Mechanical and thermomechanical properties of commercially pure chromium and chromium alloys," *Journal of Nuclear Materials*, vol. 300, no. 2-3, pp. 161–177, Feb. 2002.
- [50] X. Pang, K. Gao, F. Luo, Y. Emirov, A. A. Levin, and A. A. Volinsky, "Investigation of microstructure and mechanical properties of multi-layer Cr/Cr₂O₃ coatings," *Thin Solid Films*, vol. 517, no. 6, pp. 1922–1927, Jan. 2009.
- [51] D. H. Kam, J. H. Lee, T. Lee, and Y. H. Jeong, "Critical heat flux for SiC- and Cr-coated plates under atmospheric condition," *Annals of Nuclear Energy*, vol. 76, pp. 335–342, Feb. 2015.
- [52] J.-C. Brachet, M. Dumerval, V. Lezaud-Chaillioux, and M. Le Saux, "BEHAVIOR OF CHROMIUM COATED M5 TM CLADDINGS UNDER LOCA CONDITIONS," Sep-2017. [Online]. Available: https://www.researchgate.net/publication/319988324_Behavior_Of_Chromium_Coated_M5_Tm_Claddings_Under_Loca_Conditions.
- [53] J.-C. Brachet, I. Idarraga-Trujillo, M. L. Flem, M. L. Saux, V. Vandenberghe, S. Urvoy, E. Rouesne, T. Guilbert, C. Toffolon-Masclat, M. Tupin, C. Phalippou, F. Lomello, F. Schuster, A. Billard, G. Velisa, C. Ducros, and F. Sanchette, "Early studies on Cr-Coated Zircaloy-4 as enhanced accident tolerant nuclear fuel claddings for light water reactors," *Journal of Nuclear Materials*, vol. 517, pp. 268–285, Apr. 2019.
- [54] D. C. Roache, A. Jarama, C. H. Bumgardner, F. M. Heim, J. Walters, J. Romero, B. Maier, and X. Li, "Unveiling damage mechanisms of chromium-coated zirconium-based fuel claddings by coupling digital image correlation and acoustic emission," *Materials Science and Engineering: A*, vol. 774, no. 13, Feb. 2020.
- [55] B. K. Bae, C. S. Seok, J. M. Koo, H. I. Kim, and K. Murty, "Creep Rupture Studies of Zirlo Tubing Using Ring Tensile Specimen," *Advanced Nondestructive Evaluation I Key Engineering Materials*, pp. 565–569, Jan. 2006.
- [56] H.G. Kim, I.-H. Kim, Y.-I. Jung, D.-J. Park, J.-Y. Park, and Y.-H. Koo, "Adhesion property and high-temperature oxidation behavior of Cr-coated Zircaloy-4 cladding tube prepared by 3D laser coating," *Journal of Nuclear Materials*, vol. 465, pp. 531–539, Oct. 2015.

- [57] S.-K. Kim, J.-G. Bang, D.-H. Kim, I.-S. Lim, Y.-S. Yang, K.-W. Song, and D.-S. Kim, "Hoop strength and ductility evaluation of irradiated fuel cladding," *Nuclear Engineering and Design*, vol. 239, no. 2, pp. 254–260, Oct. 2009.
- [58] J.C. Brachet, I. Idarraga-Trujillo, M. L. Flem, M. L. Saux, V. Vandenberghe, S. Urvoy, E. Rouesne, T. Guilbert, C. Toffolon-Masclat, M. Tupin, C. Phalippou, F. Lomello, F. Schuster, A. Billard, G. Velisa, C. Ducros, and F. Sanchette, "Early studies on Cr-Coated Zircaloy-4 as enhanced accident tolerant nuclear fuel claddings for light water reactors," *Journal of Nuclear Materials*, vol. 517, pp. 268–285, Feb. 2019.
- [59] B. Cox, "Oxidation and Corrosion of Zirconium and Its Alloys," *Corrosion*, vol. 16, no. 8, Apr. 1960.
- [60] J.C. Brachet, M. Le Saux, V. Lezard-Chaillieux, M. Dumerval, Q. Houmaire. Behavior under LOCA conditions of Enhanced Accident Tolerant Chromium Coated Zircaloy-4 Claddings. Topfuel 2016 - Light Water Reactor (LWR) Fuel Performance Meeting, Sep 2016, United States.

Chapter 2: Overview of Digital Image Correlation, Acoustic Emission, Expanding Plug Testing, and 4-point Bending Testing

This chapter provides a brief overview of four key techniques used in this thesis: digital image correlation (DIC), acoustic emission (AE), expanding plug mechanical testing, and 4-point bending mechanical testing. The author notes that the majority of this chapter is taken from and adapted from an internal report produced by the author and his lab mates [1].

2.1 Digital Image Correlation Overview

Three-dimensional digital image correlation (3D-DIC) is an optical technique that uses stereoscopic images to capture spatial measurements for surface strain and displacement analysis. 3D-DIC is typically used to collect *in-situ* deformation measurements during mechanical loading (Figure 2.1), and it is the only technique used in this work to quantify deformation and strain of the coated fuel claddings under investigation [2]. Additionally, this technique is capable of measuring out-of-plane displacements with exceptional accuracy, with height measurements being shown to be accurate to $1/20,000^{\text{th}}$ of the camera-sample distance [3,4]. The key elements of accurate DIC measurements include: a high-contrast surface pattern, a pair of high-resolution digital cameras, accurate calibration to geometrically relate images from the two cameras, and a robust DIC algorithm to compute 3D position.

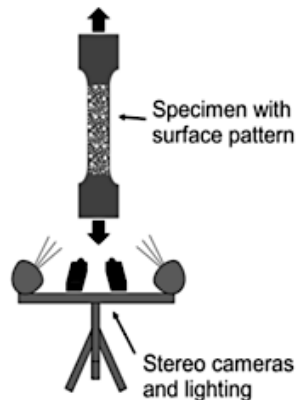


Figure 2.1: Schematic of a Typical 3D-DIC Setup. [2]

In order to quantify and track deformation of a material with 3D-DIC, the specimen being tested must have some type of random, high contrast surface pattern. This pattern can be inherent to the material itself, such as the natural grain of the material, or the pattern can be applied with paint, such as a black speckle pattern on a white background. Since the images captured with DIC are distance invariant, DIC can be applied across multiple length scales, including at the nanoscale level with high resolution transmission electron microscopy imaging [5], at the microscale level with scanning electron microscopy (SEM) [6] or optical microscopy imaging [7], and at the macroscale level with digital imaging [8]. DIC typically requires uniform illumination and a non-reflective surface pattern across these three length scales, since glare and shadows can reduce contrast and cause undersaturation or oversaturation in some regions within the field of view of the cameras. In order to reduce the error in DIC measurements, the surface pattern should produce the widest contrast range possible, such that the full range of grayscale values are used when the grayscale images are digitized.

For 3D-DIC two high-resolution digital cameras are positioned in front of the sample, such that both cameras are angled inwards towards the specimen, producing overlapping fields of view. Each camera's lens must be brought into focus on the outer surface of the specimen, and the apertures must be adjusted to maximize the apparent contrast of the pattern on the specimen. Generally, higher resolution cameras allow for finer speckle patterns, allowing for more accurate deformation data. During mechanical loading the digital cameras simultaneously capture the deformation of the specimen, and that information is digitized into grayscale values that are used to extract displacement and strain measurements from each image using the 3D-DIC software.

In order to calculate displacement in 3D space, the spatial relationship between the cameras needs to be determined first. This is achieved through calibration of the cameras with the 3D-DIC

software prior to every test. Calibration typically involves using the cameras to capture stereoscopic images of a calibration panel with a known, high contrast, uniform grid pattern that is supplied by the software company. Each grid contains special markers that allows the software to correlate the grid pattern in the images (pixels) to physical dimensions. Calibration images are taken when the calibration panel is in the focal plane of both cameras, and while the panel is slightly translated in-plane and out-of-plane. These images are transferred to the 3D-DIC software, where the spatial location of overlapping regions of the cameras are located with respect to the 2D coordinate system of each camera. These locations are compared, and common locations are triangulated to produce a complete 3D spatial map. It is important to note the 2D images alone cannot be used to quantify deformation in 3D space. The spatial relationship between the cameras found through calibration allows for out-of-plane measurements with DIC.

Once the cameras are calibrated, the 3D-DIC software can be used to determine the deformation along the surface of the tested material, by tracking and quantifying the displacement of the speckle pattern. As Figure 2.2 shows, the digital images are broken down into groups called subsets, which are used to track the local deformation of the speckles [9]. Reference subsets are derived from the first set of images taken during the start of loading. The deformed subsets from the subsequent images are compared to these reference subsets to form a displacement vector, that is used to quantify deformation. The specific size of the subset is chosen in accordance with the average speckle diameter. Smaller subset sizes result in fewer speckles, and thus less unique information, in every subset. If the subset size is too small, then the subsets could become indiscernible from other subsets. This can lead to significant gaps in the 3D spatial map or even result in complete failure of the DIC software to generate spatial data. On the other hand, if the subset size is too large, then computational time is increased while spatial resolution is decreased.

Therefore, choosing an optimal subset size will always be a compromise between computational speed and integrity of the full 3D spatial map. Although DIC has been used in a number of studies of fuel claddings to provide a full-field strain map during loading [10-12], the strain map itself is not capable of detecting individual cracks. The strain maps can be used to identify localized strain concentrations, indicating numerous cracks in that region.

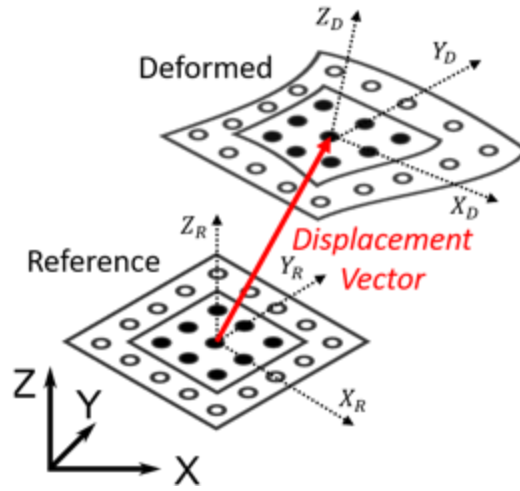


Figure 2.2: Illustration of 3D-DIC Displacement Vector between Undeformed and Deformed Subsets. [9]

3D-DIC, like all other measurement systems, intrinsically has errors, and these errors can be attributed to the image digitization process, the overall camera setup, and the overall calibration. In an extensive study by Sandia National Laboratories, these errors were separated into image correlation and calibration errors, as shown in Figure 2.3 [13]. Random noise is added to the DIC measurements when the surface of a specimen is imaged and when the images are subsequently digitized into grayscale values. Noise is also added to the DIC measurements when a poor-quality speckle pattern is used, or when a non-ideal camera setup is used, such as having uneven lighting leading to glare or having the lenses out of focus. Systematic errors that decrease the accuracy of the DIC measurements can be introduced with a poor calibration, changes to the testing

environment, or movement of the cameras. In order to obtain the most accurate and precise spatial deformation measurements with DIC, the intrinsic errors within the 3D-DIC system need to be minimized.

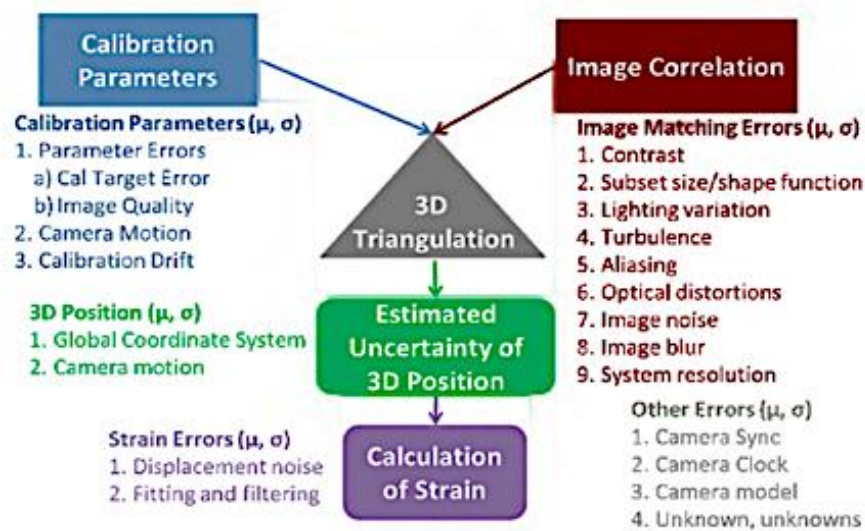


Figure 2.3: 3D-DIC Intrinsic Errors Can Be Categorized into Image Correlation and Calibration Errors; Listed Are Some Factors That Affect Each Type of Error. [13]

2.2 Acoustic Emissions to Detect Cracks

Acoustic emission (AE) measurements are a nondestructive detection technique (NDT) that have been shown to be useful for a variety of *in-situ* mechanical evaluation investigations. For example, AE techniques have been used to determine the onset and progression of crack damage between a substrate and coating in studies involving thermal barrier coatings [14-16] and nuclear fuel cladding [17,18]. Relative to the substrate thickness, coatings tend to be thin and require acoustic sensors with high sensitivity to detect sudden acoustic events. Upon yield and fracture, materials have been shown to emit significant acoustic energy events [19]. It can be assumed that the energy signals released during mechanical testing of a brittle coating on a ductile surface are indicative of coating crack initiation and crack propagation.

Acoustic events, generated from deformation or fracture, can be defined as a short pulse

above a threshold voltage as recorded by the AE sensor [20]. Many commercial AE packages, including the one used in this work, automatically record and process these AE event waveforms in real-time into a number of parameters that define the characteristics of an event signal. These parameters include peak amplitude, rise time, counts, duration and energy, and they are presented in Figure 2.4. Peak amplitude is typically measured in decibels and corresponds to how strong or loud an event is [20]. Rise time is the length of time that passed for the signal to pass a lower threshold and reach an upper threshold, typically ten percent and ninety percent of the signal strength [20]. Counts is defined as the number of times a signal crosses a threshold value, and duration is the total length of time a signal remains above a threshold value [20]. Acoustic energy is defined as the area under the waveform shape; because the magnitude of energy is related to both the peak amplitude and duration, this is often one of the best single parameters to define an event [20]. Acoustic energy is the primary acoustic parameter used in this work to evaluate the onset and propagation of coating cracking.

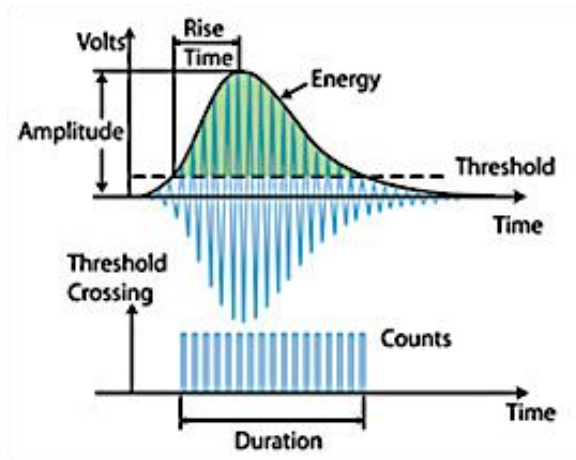


Figure 2.4: Definitions of Acoustic Event Parameters. [19]

2.3 Expanding Plug Mechanical Testing

The expanding plug mechanical test was refined by Oak Ridge National Laboratory to determine circumferential mechanical properties of tubular materials, such as fuel rod cladding

[21]. During an expanding plug test, an axial compressive load is applied to a cylindrical plug that is fitted inside a short ring of test material [21]. The axial load compresses the plug and causes the test material to expand radially. The load and radial expansion data collected during an expanding plug test can then be used to determine key mechanical properties of the test material, such as the Young's modulus and yield strength [21]. A schematic of a typical expanding plug test is shown in Figure 2.5 below. The expanding plug loading mode is of particular importance to nuclear fuel claddings, because it replicates the expansion the cladding material experiences when the nuclear fuel pellets swell during a nuclear meltdown. For this reason, the expanding plug loading mode is the primary mechanical loading mode investigated in this work.

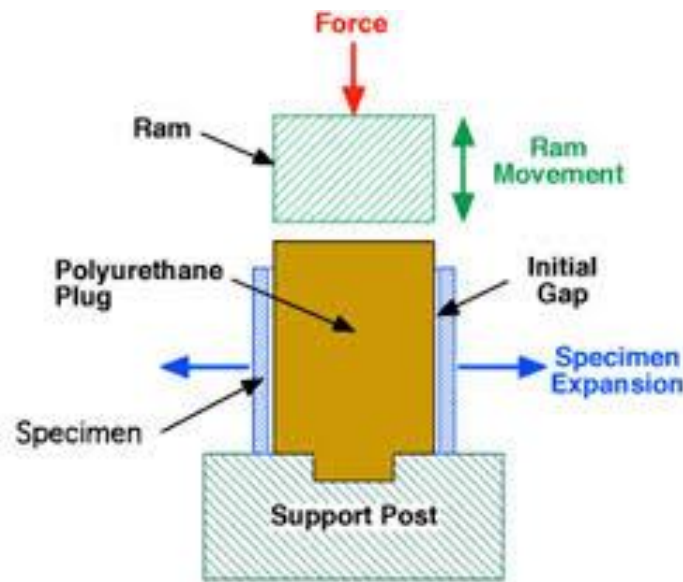


Figure 2.5: Expanding Plug Test Setup. [21]

Hoop stress in an expanding plug specimen is calculated with Equation 2.1, where P is the pressure, a is the inner radius of the tube, and b is the outer radius of the tube [22]. Pressure is the applied compressive load on the plug divided by the cross-sectional area of the plug. In this work, hoop strain is measured using the DIC software.

$$\sigma_{HOOP} = P * \frac{2a^2}{b^2 - a^2} \quad (2.1)$$

Proper alignment of the loading plungers and specimen is a key limitation of the expanding plug methodology; misalignment of the metal plungers can direct the expanding plug to one side or alter the position of the specimen relative to the plug, imparting a non-uniform σ_{HOOP} profile onto the specimen. Deformation of the exterior surface was spatially mapped using 3D-DIC to quantify strain. Alignment of the specimen with the plungers was confirmed via DIC-based displacement measurements.

2.4 Four-point Bending Mechanical Testing

During a four-point bending test, a test material is placed on two supporting pins, which are at a set distance from the center of the specimen. Two loading pins, which are also a set distance from the center of the specimen, apply load, causing the material to bend. Deformation of a bending specimen can be used to determine key material properties, such as flexural stress [23]. A schematic of a typical four-point bending test setup is shown in Figure 2.6 below [23]. Four-point bending testing was conducted to study cracking in the tensile region and to examine whether different cracking behaviors were observed across different loading modes.

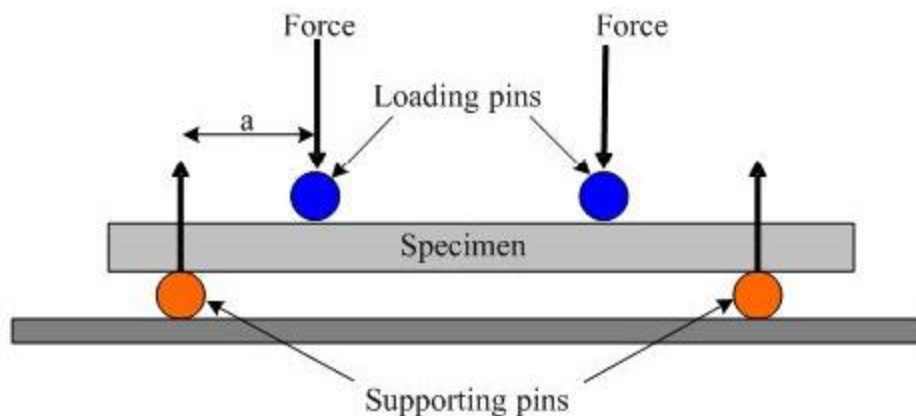


Figure 2.6: Four-point Bending Test Setup. [23]

Hoop stress in a bending specimen is calculated with Equation 2.2, where M is the bending moment, c is the radius of the test material's outer surface, and I is the moment of

inertia. The bending moment is found by multiplying the applied load by the distance between the outer and inner loading points. In this work, hoop strain is measured using the DIC software.

$$\sigma_{HOOP} = \frac{Mc}{I} \quad (2.2)$$

2.5 Summary

This chapter provided a brief overview of four key techniques used. As discussed, digital image correlation is a non-contact, optical technique used to quantify deformation to generate full-field spatial strain maps. AE techniques can be used to detect key cracking events, such as cracking onset and crack propagation, during mechanical loading. Coupling DIC and AE techniques allows spatial strain data to be correlated to key cracking events, allowing for the association of specific strain thresholds to key cracking behavior. Lastly, a brief overview on expanding plug and four-point bend mechanical testing was provided. Swelling of the nuclear fuel rod is prevalent in beyond design-basis accident conditions, and therefore, the expanding plug methodology is given the most attention in this work.

References

- [1] C. Bumgardner, F. M. Heim, D. Roache, A. Jarama, and X. Li, “Multiscale In-Situ Mechanical Testing to Evaluate Damage and Fracture of Chromium Coated Zirconium-based Fuel Claddings,” Charlottesville, VA, 2019.
- [2] B. Croom, Charlottesville, VA.
- [3] S. R. McNeill, M. A. Sutton, Z. Miao, and J. Ma, “Measurement of surface profile using digital image correlation,” *Experimental Mechanics*, vol. 37, no. 1, pp. 13–20, Mar. 1997.
- [4] M. N. Rossol, J. H. Shaw, H. Bale, R. O. Ritchie, D. B. Marshall, and F. W. Zok, “Characterizing Weave Geometry in Textile Ceramic Composites Using Digital Image Correlation,” *Journal of the American Ceramic Society*, vol. 96, no. 8, pp. 2362–2365, Dec. 2013.
- [5] Y. Sun, J. Liu, D. Blom, G. Koley, Z. Duan, G. Wang, and X. Li, “Atomic-scale imaging correlation on the deformation and sensing mechanisms of SnO₂ nanowires,” *Applied Physics Letters*, vol. 105, no. 24, p. 243105, 2014.
- [6] S. Guo, M. Sutton, X. Li, N. Li, and L. Wang, “SEM-DIC Based Nanoscale Thermal Deformation Studies of Heterogeneous Material,” *Advancement of Optical Methods in Experimental Mechanics, Volume 3 Conference Proceedings of the Society for Experimental Mechanics Series*, pp. 145–150, Aug. 2013.
- [7] C. Bumgardner, B. Croom, and X. Li, “High-temperature delamination mechanisms of thermal barrier coatings: In-situ digital image correlation and finite element analyses,” *Acta Materialia*, vol. 128, pp. 54–63, Apr. 2017.
- [8] B. P. Croom, C. Bumgardner, and X. Li, “Unveiling residual stresses in air plasma spray coatings by digital image correlation,” *Extreme Mechanics Letters*, vol. 7, pp. 126–135, Jun. 2016.
- [9] F.M. Heim, Charlottesville, VA.
- [10] P. Platt, D. Lunt, E. Polatidis, M. Wenman, and M. Preuss, “In-situ digital image correlation for fracture analysis of oxides formed on zirconium alloys,” *Corrosion Science*, vol. 111, pp. 344–351, Oct. 2016.
- [11] K. G. Field, M. N. Gussev, Y. Yamamoto, and L. L. Snead, “Deformation behavior of laser welds in high temperature oxidation resistant Fe–Cr–Al alloys for fuel cladding applications,” *Journal of Nuclear Materials*, vol. 454, no. 1-3, pp. 352–358, Nov. 2014.
- [12] L. Alva, X. Huang, G.M. Jacobsen, C. Back. High Pressure Burst Testing of SiCf-SiCm Composite Nuclear Fuel Cladding. *Advancement of Optical Methods in Experimental Mechanics, Volume 3*. 2015.

- [13] M. Phillip L. and T. J., “DIC Uncertainty Quantification for Large Scale Outdoor Testing.,” DIC Uncertainty Quantification for Large Scale Outdoor Testing. (Conference) | OSTI.GOV, 01-May-2014. [Online]. Available: <https://www.osti.gov/servlets/purl/1145766>.
- [14] K. Ono, S. Safai, and H. Herman, “Acoustic emission study of thermal-sprayed oxide coatings,” *Thin Solid Films*, vol. 63, no. 1, pp. 1-11, Oct. 1979.
- [15] K. Ito, H. Kuriki, H. Araki, S. Kuroda, and M. Enoki, “Detection of segmentation cracks in top coat of thermal barrier coatings during plasma spraying by non-contact acoustic emission method,” *Science and Technology of Advanced Materials*, vol. 15, no. 3, Jun. 2014.
- [16] K. Ito, S. Ohmata, K. Kobayashi, M. Watanabe, S. Kuroda, and M. Enoki, “Crack Monitoring during Plasma Spraying of Ceramic Coatings by Non-Contact Acoustic Emission Method,” *Materials Transactions*, vol. 51, no. 7, pp. 1272–1276, Jun. 2010.
- [17] Barrett, K., Bragg-Sitton, S., and Galicki, D., 2012, *Advanced LWR Nuclear Fuel Cladding System Development Trade-off Study*.
- [18] S. A. Nikulin, V. G. Khanzhin, A. B. Rozhnov, A. V. Babukin, and V. A. Belov, “Analysis of crack resistance and quality of thin coatings by Acoustic Emission,” *International Journal of Microstructure and Materials Properties*, vol. 1, no. 3/4, pp. 364–373, Jan. 2006.
- [19] Z. Kral, W. Horn, and J. Steck, “Crack Propagation Analysis Using Acoustic Emission Sensors for Structural Health Monitoring Systems,” 50th AIAA/ASME/ASCE/AHS/ASC Structures, Structural Dynamics, and Materials Conference, Aug. 2009.
- [20] “Acoustic Emission,” NDTT. [Online]. Available: http://www.ndttechnologies.com/products/acoustic_emissions.html.
- [21] J.-A. Wang and H. Jiang, “The Development of Expansion Plug Wedge Test for Clad Tubing Structure Mechanical Property Evaluation,” 12-Jan-2016. [Online]. Available: <https://www.osti.gov/biblio/1238021-development-expansion-plug-wedge-test-clad-tubing-structure-mechanical-property-evaluation>.
- [22] M. G. Jenkins and J. A. Salem, “Test Methods for Hoop Tensile Strength of Ceramic Composite Tubes for Light Water Nuclear Reactor Applications,” 2015. [Online]. Available: <https://ntrs.nasa.gov/archive/nasa/casi.ntrs.nasa.gov/20150009928.pdf>.
- [23] “Flexural or Bend Testing.” [Online]. Available: <https://www.touchstonetesting.com/services/material-testing/mechanical-testing/flexural-or-bend-testing/>.

Chapter 3: Overview of Room Temperature (23 °C) and High Temperature (315 °C) Testing Methodologies

This chapter provides a brief overview of the room temperature (23 °C) and high temperature (315 °C) testing methodologies used in this work. Specifics on material preparation, key mechanical testing parameters, crack characterization techniques, data processing of the acoustic emissions and DIC data, and image averaging for high temperature DIC data processing are provided. The majority of this chapter is taken from and adapted from the author's peer reviewed journal article titled "Unveiling Damage Mechanisms of Chromium-Coated Zirconium-Based Fuel Claddings by Coupling Digital Image Correlation and Acoustic Emission" published in *Materials Science and Engineering: A* [1].

3.1 Material Preparation

Mechanical testing was performed on both coated and uncoated Zr-alloy cladding specimens, which were provided by Westinghouse Electric Company. Expanding plug and four-point bending tests were conducted on all room temperature samples, while only expanding plug tests were conducted on all high temperature samples. For the coated specimens, a thin chromium coating was deposited on full length Zr-alloy claddings via a cold spraying process optimized for nuclear claddings [2-4]. The same polishing technique was applied on both coated and uncoated specimens to ensure a comparable surface. A laser micrometer was used to measure coating thickness of the room temperature specimens; average coating thickness for those room temperature specimens are listed in Tables 4.1 and 4.2 in Chapter 4. Scanning electron microscopy (SEM) imaging was used to measure the coating thickness of the high temperature samples; average coating thickness for the high temperature samples are listed in Table 5.1 in Chapter 5. Specimens were then cut down to lengths appropriate for their respective test types by a water-cooled diamond saw.

3.2 Data Capturing

In situ three-dimensional digital image correlation (3D-DIC) and acoustic emission (AE) were used concurrently with mechanical testing to measure strain field development and crack initiation and propagation during loading [5]. As stated previously, the key elements needed to acquire accurate 3D-DIC measurements include: a high-contrast surface pattern, high-resolution digital cameras, accurate calibration to geometrically relate the stereoscopic images, and a robust numerical algorithm to compute deformation measurements in 3D-space [7,8]. To achieve a high-contrast cladding surface, a random, black and white speckle pattern using conventional, matte-finish spray paints was applied to every room temperature sample. A similar speckle pattern was applied to the high temperature samples using aerospace industry grade, matte-finish spray paints. Two 5-megapixel charge-coupled device (CCD) cameras (FLIR Grasshopper) equipped with 50 mm compact lenses (Schneider Kreuznach) were used to capture stereoscopic images of the specimens during testing. Extension tubes were used during the high temperature experiments to increase the magnification of the images, in order to counteract focus issues encountered with the physical location of the cameras with the high temperature setup. All the collected images were then processed with Correlated Solutions' numerical algorithm, VIC-3D 8. As determined from DIC images taken from the samples prior to loading, DIC strain error in the room temperature tests was typically ~0.02 %, while the thermal distortion error in the high temperature samples was ~0.05 %.

Like 3D-DIC, AE is an *in situ*, nondestructive technique that has been integrated into a number of mechanical studies to determine the onset and propagation of crack damage between a substrate and coating [9-14]. Uncoated samples were tested to significant plastic deformation using both room and high temperature setups to provide an acoustic baseline comparison for the coated

samples. Any acoustic activity detected above this baseline during loading of a coated specimen is considered to be solely indicative of coating crack initiation and propagation and not indicative of damage to the substrate. An AE sensor (Mistras 1283 AE Node) was used to capture acoustic energy events of the cladding specimens during testing. For each specimen, acoustic data was normalized against the maximum AE reading for that specific specimen; normalization of the data allowed meaningful comparisons to be drawn across all the tested samples with regards to determining the onset of crack initiation. It should be noted that due to the sensitivity of the AE data from test to test, the AE technique is not able to quantify the extent of cracking. Only qualitative observations based on the trends in the acoustic data (i.e. crack onset and crack propagation) can be drawn.

3.3 Room Temperature Mechanical Testing

Room temperature mechanical tests consisted of expanding plug and four-point bending experiments. These tests were conducted at room temperature (23 °C) using an Admet eXpert 2611 table-top, universal testing machine with an 8.9 kN load cell (Admet 1210AJ-2K-B). Samples were tested to different loads, so that the degradation of the coating could be correlated to different magnitudes of strain. After mechanical testing, damage to the chromium coating was assessed via SEM.

3.3.1 Expanding Plug

Expanding plug experiments [15-17] were conducted using a set of custom mechanical plungers that compressed a 95A Shore hardness rubber plug insert to apply a uniform σ_{hoop} on the specimens (Figure 3.1a). Two uncoated specimens ('UE' ID designation) and eleven coated specimens were tested. Each specimen had a length of 12.7 mm (0.5 in) with the rubber plug insert having a length of 6.35 mm (0.25 in). As previously stated, two sets of coated specimens were

tested with the second set having a finer surface finish ('ES' ID designation) than the first ('E' ID designation). A linear loading rate of 1.0 mm/min was used for each test. The 3D-DIC cameras were placed directly in front of each specimen (Figure 3.1a).

3.3.2 Four-Point Bending

Four-point bending experiments were conducted using a custom, four-point bending rig developed for tubular specimens and inspired by a similar test rig developed by Idaho National Laboratory (Figure 3.1b) [18,19]. This setup was in accordance with ASTM standards for tubular specimens [20,21]. For all tests, the support span (L in Figure 3.1b) was 84 mm and the load span ($L/2$ in Figure 3.1b) was 42 mm. A linear loading rate of 0.5 mm/min was used for all bending tests. In total, six specimens were tested: three uncoated ('UB' ID designation) and three coated ('B' ID designation). An AE sensor was clamped directly on one end of the specimen, away from any of the loading points, to ensure minimal interference. Unlike the expanding plug tests, in which the exact location of cracking could not be determined before testing, crack initiation during a typical four-point bend test was expected to occur on the underside of the specimen as that is the area that exhibits the highest tensile strain during loading. Therefore, the DIC cameras were placed in front of and below the specimen and angled upwards to fully capture the underside of the cladding.

3.4 High Temperature Mechanical Testing

High temperature tests consisted of two uncoated ('UHT' ID designation) and five coated ('HT' ID designation) expanding plug tests. These tests were conducted at 315 °C using an Admet eXpert 2654 universal testing machine with a 100 kN load cell. A custom-made high temperature box furnace (SentroTech-1600C-666) compatible with the 100kN test frame was manufactured to replicate the room temperature loading setup at temperature. The furnace has a

maximum continuous operating temperature of 1600 °C and has two openings (one on top and one on the bottom), through which two zirconia loading platens could be positioned for loading (Figure 3.2). The sample would be placed on the loading platens for calibration of the DIC cameras prior to heating up of the furnace. The temperature inside the furnace was verified with the furnace’s built-in thermocouples and an infrared camera, which was positioned behind the cameras and angled towards the sample, prior to loading of each sample.

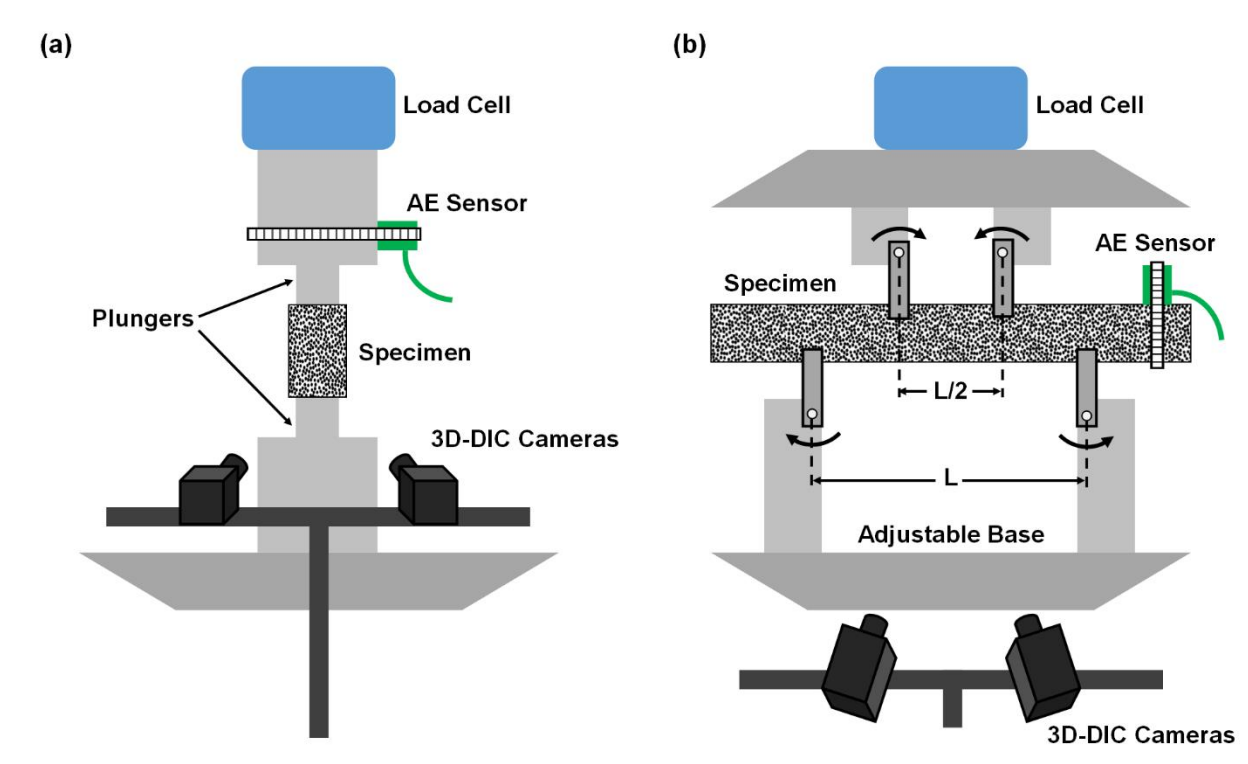


Figure 3.1: Schematic of a Typical (a) Expanding Plug and (b) Four-point Bend Test Setup. [1]

Each specimen had a length of 19.1 mm (0.75 in) with an aluminum plug insert having a length of 6.35 mm (0.25 in). A different plug material needed to be used in this case, because the melting point of the rubber plugs is below the testing temperature for these high temperature experiments. A linear loading rate of 1.0 mm/min was used for each test. The 3D-DIC cameras were placed directly in front of each specimen (Figure 3.2) to capture as much of the specimen as possible. The high temperature samples were tested to different magnitudes of strain, in order to

measure the degradation of the coating. As with the room temperature samples, damage to the coating of the high temperature samples was assessed via SEM.

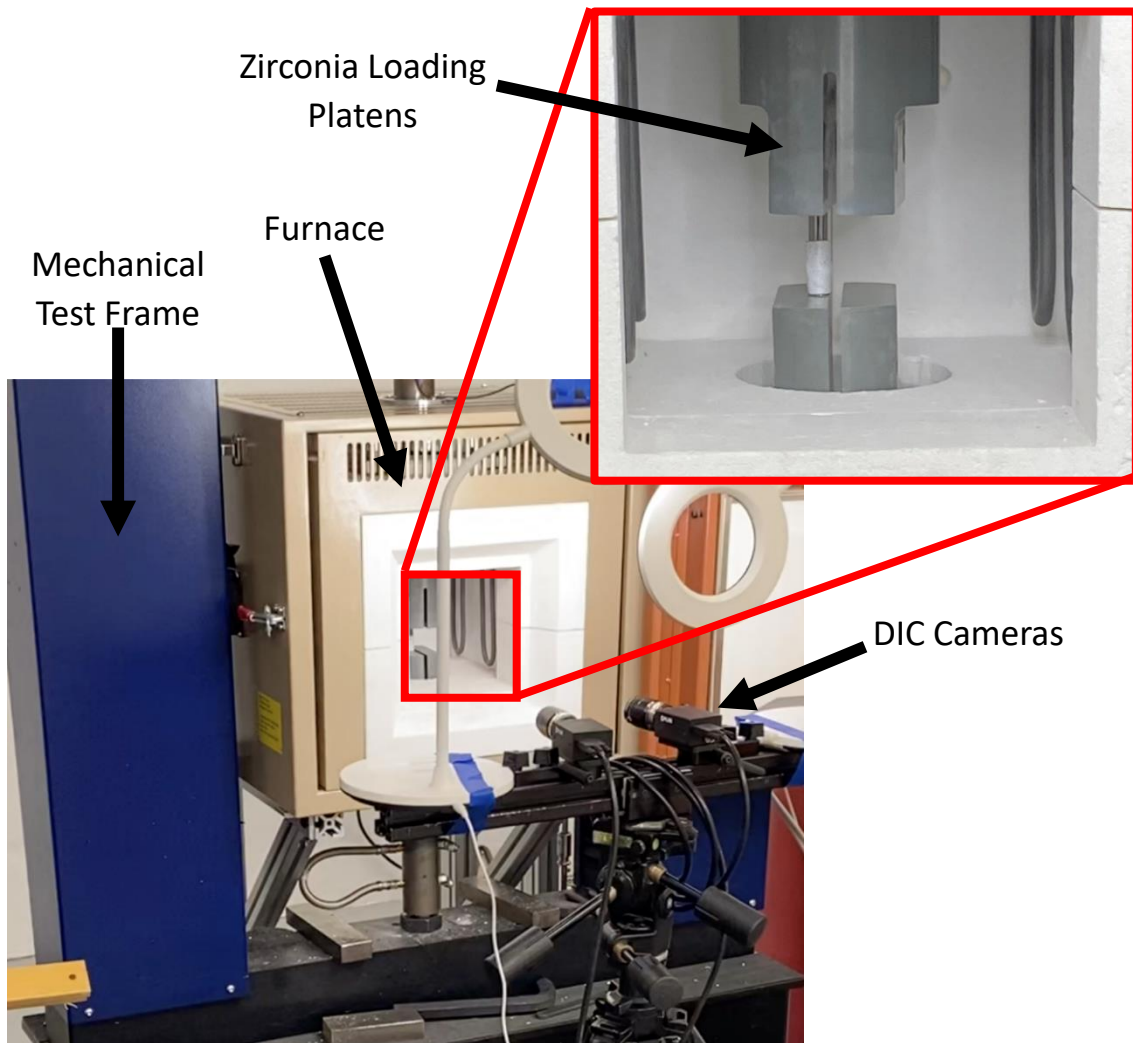


Figure 3.2: Schematic of a High Temperature Expanding Plug Test Setup.

3.5 Crack Characterization

After mechanical testing, the surface paint was removed using acetone for the room temperature specimens and using aircraft paint remover for the high temperature specimens. SEM imaging was performed on the coating surface of select specimens to assess coating damage. Select expanding plug specimens were chosen for cross-sectional SEM imaging based on their respective maximum incurred ϵ_{hoop} . These specimens were cut where expansion was greatest and where

coating cracking was expected to be most severe, using a water-cooled, circular-bladed diamond saw. Each specimen's cross-sectional area was then polished and imaged under SEM in order to verify and correlate the extent of coating cracking with the measured strain. As explained in Chapter 5, extensive SEM imaging of the high temperature samples could not be achieved due to the recent coronavirus pandemic.

3.6 Acoustic Emissions Data Processing

The author notes that the majority of this section is taken from and adapted from an internal report produced by the author and his lab mates [22].

Acoustic energy data was collected with the AE capture software and then exported to Python for processing. The start and end times of all the data streams (DIC, AE, and load) were first synced before any processing occurred. This AE raw data was then analyzed to extract the acoustic energy measurements for normalization. Normalizing the acoustic energy data made comparisons from test to test more meaningful and addressed any possible magnitude variation stemming from differences in AE sensor mounting from test to test. The cumulative total of acoustic energy events at each time step, A_i , was determined with Equation 3.1.

$$A_i = \sum_{i=0}^n a_i \quad (3.1)$$

a_i is the acoustic energy at time step i out of n total time steps (data points). The normalized quantity, N_j , was determined with Equation 3.2

$$N_i = \frac{A_i}{A_n} \quad (3.2)$$

A_n is the total cumulative acoustic energy for the duration of the entire test. At this point, the acoustic data was fully processed, and specific points of interest could be extracted for comparisons between tests. It should be noted that this data is not capable of resolving the exact locations of coating cracking. In addition, the thermal distortion in the high temperature data

increases the correlation error of the acoustic data with the DIC strain measurements. As shown in Chapter 5, the distortion error is apparent at low strains (below $\sim 0.4\%$), because the distortion error ($\sim 0.05\%$), in comparison to the DIC strain measurements, is relatively high and becomes significant. As a result, the correlation of the DIC strain measurements to key acoustic events, such as cracking onset and cracking propagation, becomes challenging due to the heat distortion.

3.7 Digital Image Correlation Data Processing

The author notes that the majority of this section is taken from and adapted from an internal report produced by the author and his lab mates [22].

DIC strain data was exported from the Vic-3D software suite in CSV format for every pair of images acquired. Strain data was imported to Python as one data array per time step. Each data array contained data for every pixel position from the pair of images; this data included x , y , and z position (mm units); u , v , and w displacement (corresponding to x , y , z directions, respectively); and ε_{xx} , ε_{yy} , ε_{xy} strain. To obtain a singular value for reporting strains in non-spatial graphical form, the average of the top ninety-five percentile of reported DIC strains was taken; this is the origin of the singular strain values reported for expanding plug at each time step. For bending, strain arrays were manually cropped down to only include data within the area between the top two loading locations; then the average of the top ninety-five percentile was taken from the cropped data.

For the bend tests, due to the positioning of the cameras below the specimen axis, these arrays were subsequently analyzed to extract the camera-to-sample angle, *i.e.*, the position of the cameras below horizontal from which they would look up at the specimen. Python code was developed to process all the data arrays, tracking specimen displacement in the y and z directions. If the camera was located at an angle of 0° , the camera would be looking straight onto the

specimen, and all specimen displacement would occur in the y direction. In these tests, the camera was located below horizontal, looking up at the specimen, so relative to the camera the specimen displacement would be shown as having y and z dimensions. The angle of the cameras was determined with Equation 3.3.

$$\theta_i = \tan^{-1}\left(\frac{w_i}{v_i}\right) \quad (3.3)$$

θ_i is the camera angle at every time step, and v_i and w_i are the specimen displacements in y and z, respectively. It was generally observed that the camera angle converged to a value over time, and that value was used to rotate the displacements and strains to a typical, horizontal reference frame. Calculating the camera angle and rotating the reference frames with the bend data greatly accelerated post-processing in VIC-3D.

3.8 Image Averaging for High Temperature Testing

Mechanical testing at elevated temperatures introduces distortion in the captured digital images. Image distortion at high temperatures is caused by convective air currents, and the distortion effect on the DIC images is as random as the convective currents themselves. This distortion effect is well documented in literature, and some of those effects on the DIC surface profile can be seen in Figure 3.3 [23]. There are a number of ways to mitigate the effects of distortion on the DIC images, such as imaging through a window, introducing a fan to direct convective air currents away from the DIC cameras, using a faster acquisition speed to collect images, and image averaging [24]. These four options were tested, and it was determined that the last two options worked best with this specific setup to counteract the heat distortion effects.

A moving average filter (Equation 3.4) was applied to all the DIC images for each high temperature expanding plug test. The images from each test were split up into overlapping sets of 20 images. The pixel position across all 20 images in each set was averaged to assemble an

averaged image. The next image set begins 5 images over from the previous set and the process repeats until all the overlapping sets are averaged. This would mean that Set 1 contains Images 1-20, Set 2 contains Images 6-25, and Set 3 contains Images 11-30. Each set results in an averaged image for DIC processing. Equation 3.4 represents the averaging of an image set to produce an averaged image, $Image_{AVG}$. N is the number of images in each set, which in this case is 20.

$$Image_{AVG} = \frac{\sum_1^N Image}{N} \quad (3.4)$$

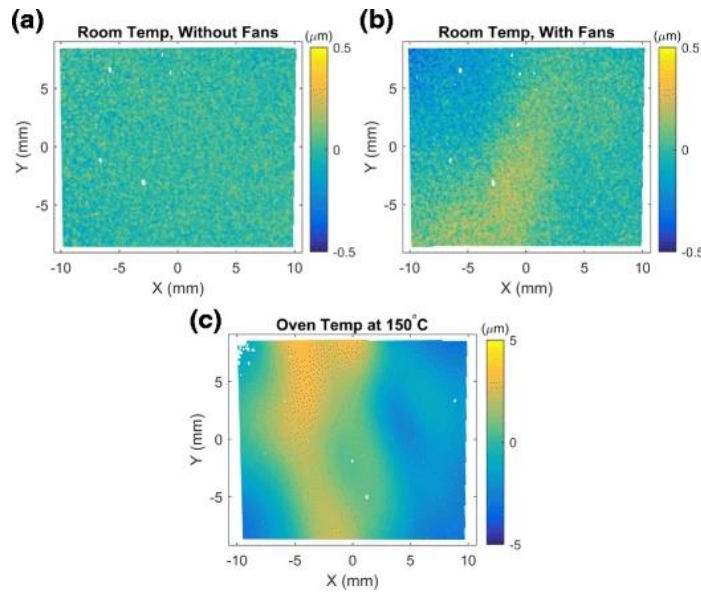


Figure 3.3: Example of DIC Image Distortion Effects on Surface Profile due to Convective Currents. [23]

Image averaging reduces the number of images available for data processing, and thus reduces the amount of data points that can be attained to correlate strain with load and acoustic data. In order to counteract this, the image acquisition rate was increased from 5 Hz (acquisition rate at room temperature) to 20 Hz. Figure 3.4a shows the effects of image averaging on the resulting hoop stress vs. hoop strain curve. From DIC images taken prior to loading, the thermal distortion in the images was determined to be $\sim 0.05\%$. As shown in Chapter 5, the thermal distortion is significant at lower strains (below $\sim 0.4\%$), and complicates the correlation strain

data to key acoustic events, such as the onset of cracking. However, it is clear that averaging reduces the overall noise in the data, while at the same time maintaining the general stress-strain trend. Figure 3.4b shows the hoop strain distribution (error) at the start of the test for a representative high temperature sample after image averaging. Combining these two techniques allowed for accurate DIC strain data acquisition at elevated temperatures.

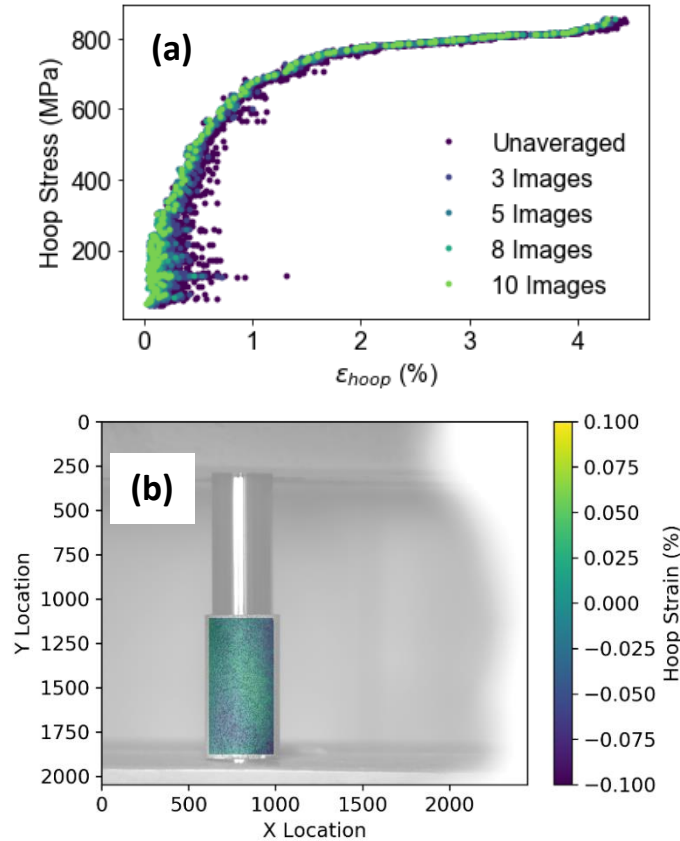


Figure 3.4: Effect of Image Averaging on (a) Hoop Stress vs. Hoop Strain Curve and (b) Hoop Strain Error.

3.9 Summary

This chapter provided a brief overview of the key methodologies used throughout the work presented in this thesis. Specifics on the tested material, application of the speckle pattern, and DIC and AE equipment used were provided. Key details regarding the room temperature and high temperature testing rigs were also addressed. DIC and AE data processing procedures were

outlined in this section. As discussed, DIC was used to quantify the deformation of the samples, while AE was used to detect the onset of coating cracking and crack propagation. Correlating the DIC strain maps to the AE data allows for specific acoustic events, such as crack onset, to be attributed to certain strain thresholds. This key association provides key metrics to relate the extent of deformation to the integrity of the coating. The key limitations of DIC and AE at room temperature and high temperature are summarized in Table 3.1 below. This proposed setup serves as an effective way to not only determine the effectiveness of coated fuel claddings, but also reveal the key fracture mechanisms of these coated claddings at different temperatures to inform future design of coated fuel claddings.

Table 3.1: Summary of DIC and AE Methodologies.

	Methodology	Purpose	Resolution	Limitations
Room Temperature	DIC	-Quantify deformation during expanding plug and four-point bend tests.	-DIC strain error is ~0.02 %.	-Accuracy is dependent on calibration and imaging matching errors. -Individual cracks cannot be detected.
	AE	-Detect onset of cracking and crack propagation.	-AE data is normalized to the sum of all AE events to enable comparisons across tests.	-Cannot resolve the location of cracking. -Sensitivity of AE data can vary test to test.
High Temperature	DIC	-Quantify deformation during expanding plug tests.	-Thermal distortion error is ~0.05 %.	-Same limitations as room temperature application. -Thermal distortion is significant at low strains.
	AE	-Detect onset of cracking and crack propagation.	- AE data is normalized to the sum of all AE events to enable comparisons across tests.	- Same limitations as room temperature application. -Large DIC thermal distortion increases the correlation error with DIC strain measurements.

References

- [1] D. C. Roache, A. Jarama, C. H. Bumgardner, F. M. Heim, J. Walters, J. Romero, B. Maier, and X. Li, “Unveiling damage mechanisms of chromium-coated zirconium-based fuel claddings by coupling digital image correlation and acoustic emission,” *Materials Science and Engineering: A*, vol. 774, no. 13, Feb. 2020.
- [2] B. Maier, H. Yeom, G. Johnson, T. Dabney, J. Walters, J. Romero, H. Shah, P. Xu, and K. Sridharan, “Development of Cold Spray Coatings for Accident-Tolerant Fuel Cladding in Light Water Reactors,” *Jom*, vol. 70, no. 2, pp. 198–202, Nov. 2017.
- [3] B. Maier, H. Yeom, G. Johnson, T. Dabney, J. Walters, P. Xu, J. Romero, H. Shah, and K. Sridharan, “Development of cold spray chromium coatings for improved accident tolerant zirconium-alloy cladding,” *Journal of Nuclear Materials*, vol. 519, pp. 247–254, Jun. 2019.
- [4] H. Shah, J. Romero, P. Xu, R. Oelrich, J. Walters, J. Wright, and W. Gassmann, “Westinghouse-Exelon EnCore® Fuel Lead Test Rod (LTR) Program including Coated cladding Development and Advanced Pellets ,” 2018. [Online]. Available: <https://www.euronuclear.org/archiv/topfuel2018/fullpapers/TopFuel2018-A0145-fullpaper.pdf>.
- [5] M. Zhou, W. Yao, X. Yang, Z. Peng, K. Li, C. Dai, W. Mao, Y. Zhou, and C. Lu, “In-situ and real-time tests on the damage evolution and fracture of thermal barrier coatings under tension: A coupled acoustic emission and digital image correlation method,” *Surface and Coatings Technology*, vol. 240, pp. 40–47, Feb. 2014.
- [6] J. Zhu, H. Xie, Z. Hu, P. Chen, and Q. Zhang, “Residual stress in thermal spray coatings measured by curvature based on 3D digital image correlation technique,” *Surface and Coatings Technology*, vol. 206, no. 6, pp. 1396–1402, Dec. 2011.
- [7] S. R. Mcneill, M. A. Sutton, Z. Miao, and J. Ma, “Measurement of surface profile using digital image correlation,” *Experimental Mechanics*, vol. 37, no. 1, pp. 13–20, Mar. 1997.
- [8] M. N. Rossol, J. H. Shaw, H. Bale, R. O. Ritchie, D. B. Marshall, and F. W. Zok, “Characterizing Weave Geometry in Textile Ceramic Composites Using Digital Image Correlation,” *Journal of the American Ceramic Society*, vol. 96, no. 8, pp. 2362–2365, Jul. 2013.
- [9] K. Ono, S. Safai, and H. Herman, “Acoustic emission study of thermal-sprayed oxide coatings,” *Thin Solid Films*, vol. 63, no. 1, Oct. 1979.
- [10] K. Ito, S. Ohmata, K. Kobayashi, M. Watanabe, S. Kuroda, and M. Enoki, “Crack Monitoring during Plasma Spraying of Ceramic Coatings by Non-Contact Acoustic Emission Method,” *Materials Transactions*, vol. 51, no. 7, pp. 1272–1276, Jun. 2010.

- [11] K. Ito, H. Kuriki, H. Araki, S. Kuroda, and M. Enoki, "Detection of segmentation cracks in top coat of thermal barrier coatings during plasma spraying by non-contact acoustic emission method," *Science and Technology of Advanced Materials*, vol. 15, no. 3, Jun. 2014.
- [12] L. Yang, T. Yang, Y. Zhou, Y. Wei, R. Wu, and N. Wang, "Acoustic emission monitoring and damage mode discrimination of APS thermal barrier coatings under high temperature CMAS corrosion," *Surface and Coatings Technology*, vol. 304, pp. 272–282, Oct. 2016.
- [13] E. Munch, L. Duisabeau, M. Fregonese, and L. Forunier, "Acoustic Emission Detection of Environmentally Assisted Cracking In Zircaloy-4 Alloy," 2004. [Online]. Available: https://inis.iaea.org/collection/NCLCollectionStore/_Public/36/105/36105030.pdf.
- [14] S. A. Nikulin, V. G. Khanzhin, A. B. Rozhnov, A. V. Babukin, and V. A. Belov, "Analysis of crack resistance and quality of thin coatings by Acoustic Emission," *International Journal of Microstructure and Materials Properties*, vol. 1, no. 3/4, Dec. 2006.
- [15] B. P. Croom, P. Xu, E. J. Lahoda, C. P. Deck, and X. Li, "Quantifying the three-dimensional damage and stress redistribution mechanisms of braided SiC/SiC composites by in situ volumetric digital image correlation," *Scripta Materialia*, vol. 130, pp. 238–241, Mar. 2017.
- [16] T. Byun, E. Lara-Curzio, R. Lowden, L. Snead, and Y. Katoh, "Miniaturized fracture stress tests for thin-walled tubular SiC specimens," *Journal of Nuclear Materials*, vol. 367-370, pp. 653–658, Aug. 2007.
- [17] H. Jiang and J.-A. J. Wang, "Methodology for mechanical property testing of fuel cladding using an expanding plug wedge test," *Journal of Nuclear Materials*, vol. 446, no. 1-3, pp. 27–37, Mar. 2014.
- [18] I.J. van Rooyen, W.R. Lloyd, T.L. Trowbridge, S.R. Novascone, K.J. Wendt, and S.M. Bragg-Sitton, "SiC-CMC-Zircaloy-4 Nuclear Fuel Cladding Performance during 4-Point Tubular Bend Testing," in *LWR Fuel Performance Meeting/Top Fuel 2013*, 2013.
- [19] C. H. Bumgardner, F. M. Heim, D. C. Roache, A. Jarama, P. Xu, R. Lu, E. J. Lahoda, B. P. Croom, C. P. Deck, and X. Li, "Unveiling hermetic failure of ceramic tubes by digital image correlation and acoustic emission," *Journal of the American Ceramic Society*, vol. 103, no. 3, pp. 2146–2159, Oct. 2019.
- [20] "Standard Test Method for Flexural Strength of Advanced Ceramics at Ambient Temperature," 10-Mar-2002. [Online]. Available: <https://reference.globalSpec.com/standard/3809053/astm-c1161-02>.

- [21] “Standard Test Method for Flexural Properties of Unreinforced and Reinforced Plastics and Electrical Insulating Materials by Four-Point Bending,” 2010. [Online]. Available: <https://www.astm.org/Standards/D6272.htm>.
- [22] C. Bumgardner, F. M. Heim, D. Roache, A. Jarama, and X. Li, “Multiscale In-Situ Mechanical Testing to Evaluate Damage and Fracture of Chromium Coated Zirconium-based Fuel Claddings,” Charlottesville, VA, 2019.
- [23] E. M. C. Jones and P. L. Reu, “Distortion of Digital Image Correlation (DIC) Displacements and Strains from Heat Waves,” *Experimental Mechanics*, vol. 58, no. 7, pp. 1133–1156, Jul. 2018.
- [24] B. P. Croom, C. Bumgardner, and X. Li, “Unveiling residual stresses in air plasma spray coatings by digital image correlation,” *Extreme Mechanics Letters*, vol. 7, pp. 126–135, Jun. 2016.

Chapter 4: Failure Mechanisms at Room Temperature (23 °C)

This chapter presents the key results from the room temperature (23 °C) mechanical testing conducted on the chromium-coated fuel cladding samples. Hoop strain and acoustic data are presented for each sample, in addition to SEM images of coating cracking from select samples. The majority of this chapter is taken from and adapted from the author’s peer reviewed journal article titled “Unveiling Damage Mechanisms of Chromium-Coated Zirconium-Based Fuel Claddings by Coupling Digital Image Correlation and Acoustic Emission” published in *Materials Science and Engineering: A* [1].

3D-DIC and AE were coupled to capture coating crack progression during expanding plug and four-point bending tests at room temperature. 3D-DIC was used to generate global strain maps of each specimen during loading, and the recorded peak strains for each specimen are listed in Table 4.1 for expanding plug and Table 4.2 for four-point bending. AE detection was used to establish a baseline comparison between uncoated and coated samples, such that any acoustic signal above this baseline was assumed to be indicative of coating cracking. Areas with the highest strain concentrations were targeted with subsequent SEM imaging, since these areas were likely the sites of crack initiation. Combining DIC measurements and AE monitoring allowed key coating cracking events to be correlated, such as crack onset, with DIC deformation measurements.

Table 4.1: Coating Thickness and Max Hoop Strain of Expanding Plug Specimens

Test Type	Specimen ID	Average Coating Thickness (μm)	Max ε_{hoop} (%)
Expanding Plug	UE01	0	5.3
	UE02	0	7.0
	E01	45	0.26
	E02	42	0.38
	E03	45	0.44
	E04	42	0.48
	E05	30	5.7

	E06	30	6.2
	ES01	35	0.44
	ES02	35	0.56
	ES03	35	0.8
	ES04	35	1.4
	ES05	35	2.4

Table 4.2: Coating Thickness and Max Bending Strain of Four-point Bend Specimens

Test Type	Specimen ID	Average Coating Thickness (μm)	Max ϵ_{xx} (%)
Four-Point Bending	UB01	0	1.6
	UB02	0	1.9
	UB03	0	2.6
	B01	50	0.4
	B02	62	0.5
	B03	35	1.1

4.1 Room Temperature Mechanical Testing

Graphical results presented for each specimen include both stress and normalized cumulative acoustic energy plotted against strain in the relevant reference configuration (ϵ_{hoop} for expanding plug, ϵ_{xx} for four-point bend) for each test. Specimens are numbered in ascending order based on the maximum recorded strain of the sample. 3D-DIC was used to generate spatial strain maps for each specimen during deformation; these strain maps and the corresponding acoustic data were used to identify areas of high strain where cracking was likely to occur.

4.1.1 Expanding Plug

Two uncoated Zr-alloy expanding plug samples were first tested to establish a baseline acoustic signal unassociated with coating cracking. The two uncoated claddings were both loaded beyond yielding and achieved maximum ϵ_{hoop} greater than 5 %. No significant acoustic energy events were detected during testing of the uncoated expanding plug specimens, indicating that acoustic energy signals detected during testing of coated specimens were attributed to the

degradation of the coating itself, rather than being associated with damage to the cladding or with excessive background noise.

Each coated cladding specimen was tested to varying loads; the load was subsequently correlated to the DIC-measured hoop strain to assess coating cracking onset and degradation with increasing deformation of the specimen. For the E specimens, maximum ϵ_{hoop} ranged from 0.26 % to 6.2 %, and the maximum applied load ranged from around 3000 N to 7000 N. The first significant acoustic event regularly occurred around 0.4 % ϵ_{hoop} (Figure 4.1b). After the initial acoustic energy event, many AE events quickly followed, resulting in a consistent, linear increase in the normalized cumulative acoustic energy. The rate of AE events was steady until around 0.6 % ϵ_{hoop} , at which point the AE signals began to decrease. It is suspected that the initial sharp rise in AE activity was associated with crack initiation around the circumference of the specimen. In addition, it is expected that the decrease in the rate of acoustic activity corresponds to crack saturation with subsequent acoustic activity corresponding to crack propagation rather than initiation. Similar behavior has been seen in other studies which have incorporated AE techniques [2,3,4]. Furthermore, this sharp rise in AE activity points to a sudden burst of cracking all around the circumference of the specimen rather than a gradual onset of cracking. This observation is affirmed by the DIC strain profiles (Figure 4.2), in which high strains are concentrated over the entire center band of the specimens, and by the SEM imaging presented in Section 4.2.

The ES specimens were also loaded to increasing levels of ϵ_{hoop} and exhibited similar acoustic trends as the E specimens (Figure 4.1c, d). During these tests, the first significant acoustic event regularly occurred around 0.4 % ϵ_{hoop} , again similar to the E specimens (Figure 4.1a, b). Unlike the E specimens, the ES specimens all had the same coating thickness (35 μm). This coating uniformity likely led to the decreased variation in ϵ_{hoop} associated with the onset of cracking, and

thus suggests that the *onset of coating cracking* may be influenced by the thickness and surface finish of the chromium coating. However, it was also observed for the ES specimens that the rate of acoustic activity following crack initiation, which is reflected by the slope of the normalized AE data, was largely consistent among the E specimens, indicating that the *rate of crack propagation* associated with through thickness cracking is largely unaffected by coating thickness or surface finish of the sample.

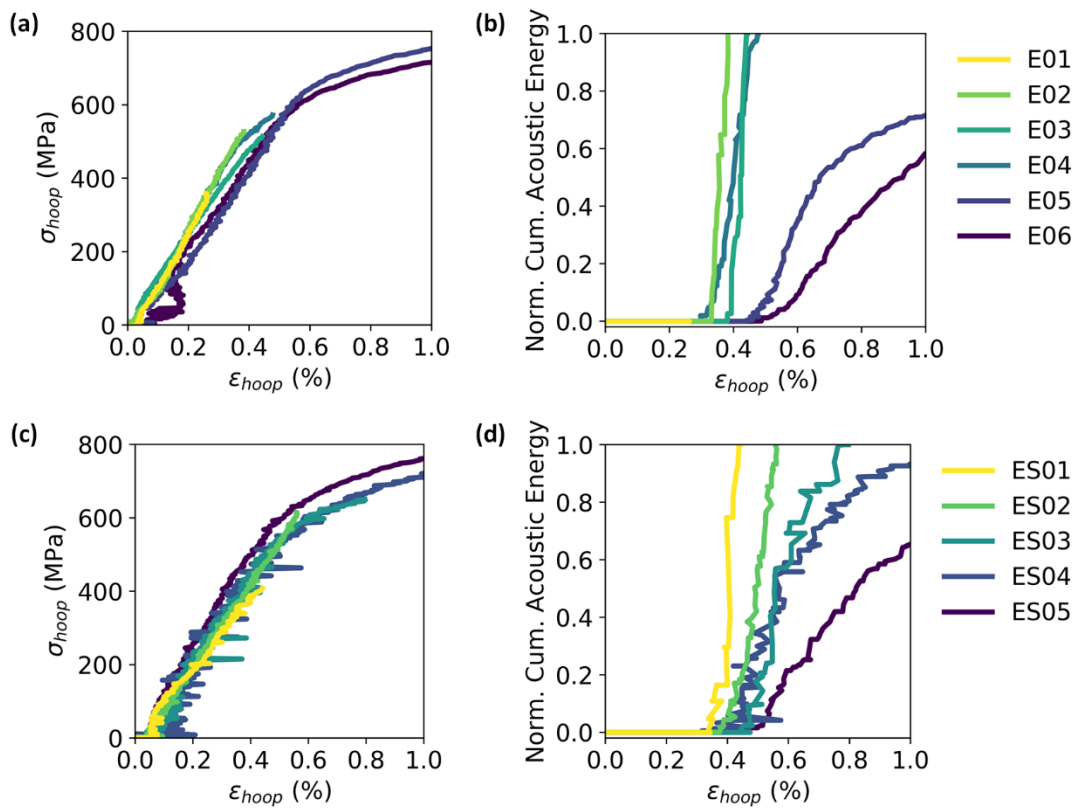


Figure 4.1: σ_{hoop} vs. ϵ_{hoop} for (a) E and (c) ES specimens and Normalized Cumulative Acoustic Energy vs. ϵ_{hoop} for (b) E and (d) ES specimens. [1]

Representative DIC strain maps of ES04, illustrating the progression of deformation during key acoustic events, are presented in Figure 4.2. As loading progressed, the expansion of the plunger resulted in the development of a strain band along the center of the specimen (Figure 4.2d). Cracks within the specimen were too small ($\ll 1$ pixel) and too closely spaced to distinguish

individual crack openings with 3D-DIC, thus requiring subsequent SEM imaging to verify and characterize coating cracking. Localized strain concentrations picked up by 3D-DIC during loading, however, can be attributed to the aggregate effect of the opening of multiple cracks in that specific region.

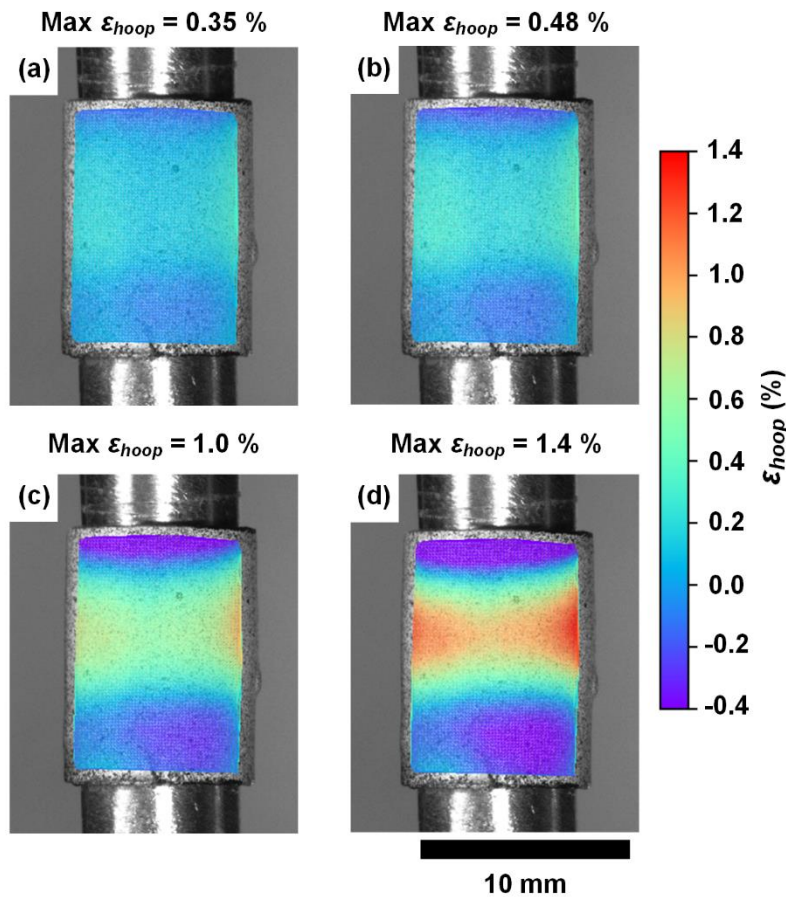


Figure 4.2: Typical Spatial ϵ_{hoop} Progression During an Expanding Plug Test, Here for ES04, at (a) First AE Event, (b) First Significant AE Event, (c) Second Cluster of AE Events, and (d) at Test Endpoint. [1]

4.1.2 Four-point Bending

Results from the coated four-point bending tests are shown in Figure 4.3. As with the uncoated expanding plug specimens, three uncoated bending specimens were loaded beyond yielding in excess of $1.6\% \epsilon_{xx}$ and as high as $2.6\% \epsilon_{xx}$. No AE events were detected during loading

of the uncoated bending samples, indicating again that any acoustic activity recorded during testing of the coated specimens was evidence of coating cracking. The coated specimens were tested to loads ranging from 1500 to 3000 N, which corresponded to maximum ϵ_{xx} ranging from 0.4 to 1.1 %. The first AE signals occurred between 0.35 and 0.45 % ϵ_{xx} . B01 and B02 exhibit sharp rises in normalized cumulative acoustic energy, because both of these specimens were loaded until the onset of coating cracking. B03, on the other hand, was loaded to higher strains and exhibited a consistent, linear rise in normalized cumulative acoustic energy. Similar to the expanding plug specimens, this acoustic trend is evidence of coating crack initiation and propagation along the surface of the bending specimens.

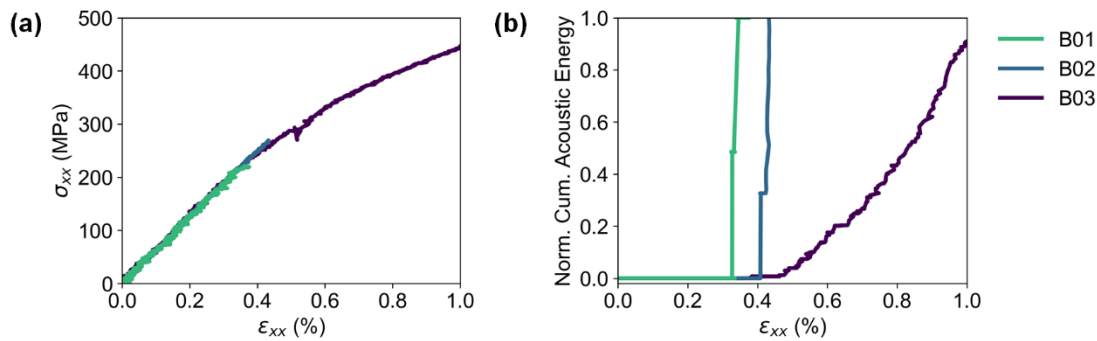


Figure 4.3: (a) σ_{xx} vs. ϵ_{xx} and (b) Normalized Cumulative Acoustic Energy vs. ϵ_{xx} . [1]

Figure 4.4 illustrates the progression of deformation during key acoustic events for B03. Since B03 was tested to the highest ϵ_{xx} among the coated specimens, the strain profiles of the other coated bending specimens are captured and well represented in Figure 4.4. The strain profile before the first acoustic event, as shown in Figure 4.4a, is uniform with a maximum ϵ_{xx} around 0.2 %. Figure 4.4b shows the strain profile when the first acoustic events were detected at around a maximum ϵ_{xx} of 0.49 %. The strain profile reflects a typical Euler-Bernoulli beam-in-bending profile, transitioning to tensile strains along the underside of the specimen and to compressive strains above. As strains increased to a maximum ϵ_{xx} of 0.72 % in Figure 4.4c, localized strain

bands formed along the underside of B03. These localized strain regions may be evidence of multiple crack formations or crack openings along the transverse direction of the specimen; however, this cracking behavior was unable to be confirmed with SEM imaging since grinding striations were present along the same direction as cracking. As shown in Figure 4.4d, with further loading of B03 to a peak ϵ_{xx} of 1.1 %, it was no longer possible to identify any localized strain concentrations, similar to the highly strained expanding plug specimens. In a four-point bend test, the underside of the specimen experienced the highest tensile strains and likely the most cracking; this region was therefore targeted during SEM imaging.

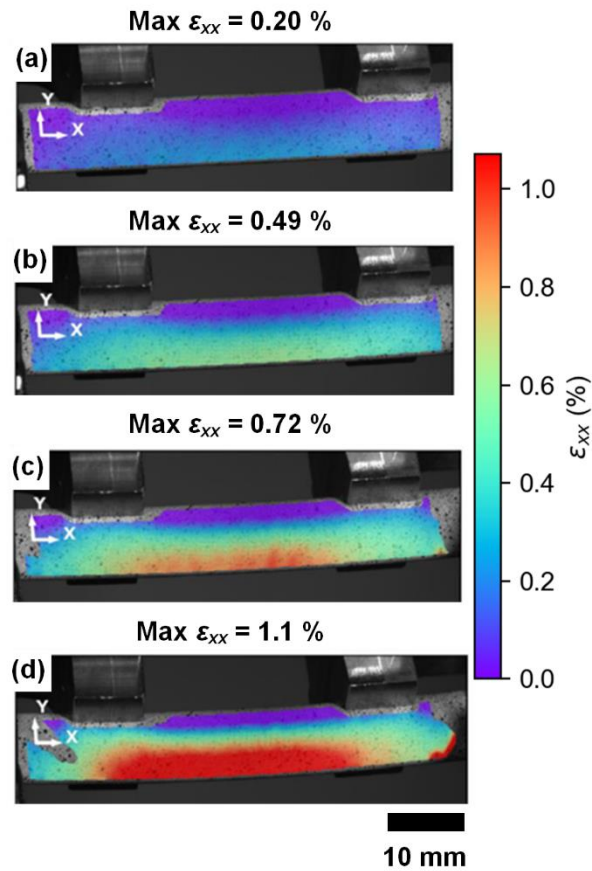


Figure 4.4: Typical Spatial Strain Progression During a Four-point Bend Test, Here for B03, at (a) 0.2% ϵ_{xx} , (b) First Significant AE Event, (c) Crack Opening during AE Cluster, and (d) at Test Endpoint. [1]

4.2 Room Temperature Crack Characterization

In general, localized strain regions in the DIC strain maps were indicative of regions with multiple coating crack openings in the fuel cladding samples. Since 3D-DIC was not capable of detecting the opening of individual cracks, SEM imaging was used to confirm the existence of cracks in the coating for select specimens of each test type. This combination of 3D-DIC and SEM imaging allowed for coating damage to be correlated with the maximum strains for each tested specimen.

4.2.1 Expanding Plug

Upon examination of the E specimens under SEM, grinding marks from the coarser surface finish were found running along the transverse direction. Each specimen had axial cracks along the central band of high ϵ_{hoop} concentrations, as shown in Figure 4.5a. These axial cracks were widest along the center of the specimen where the hoop strain concentration was greatest and where cracking most likely initiated before expanding axially. The axial cracks were typically spaced uniformly across the circumference of each specimen and were fairly uniform in length, tapering gradually as they traveled farther from the centralized strain bands. The uniform distribution of cracks around the surface has been reported in the literature for similar loading methods [5], and is likely attributed to the uniform band of strain in the bulged region illustrated in the DIC strain maps (Figure 4.2d). Despite the transverse grinding striations and pits found throughout the coating, no evidence was found indicating that these striations and pits had a significant impact on the overall pathway of the axial cracks. Cracks continued to propagate straight down the specimen's axis, even in the presence of these striations and pits. This behavior reinforces a greater dependence on the applied strain and deformation rather than surface finish or other structural features for the expanding plug loading mode.

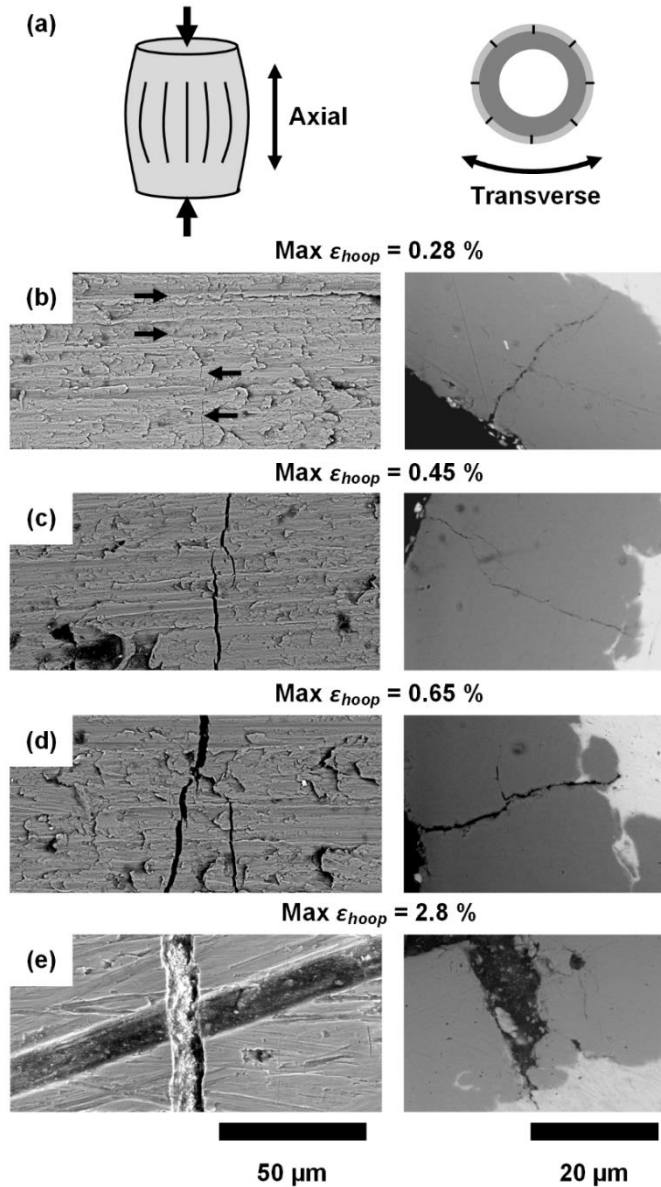


Figure 4.5: Representative SEM Images at the Surface (Left) and Cross-section (right) for Expanding Plug Specimens: (a) Schematic of the Loading/Cracking Conditions and the Specimen Orientation, (b-e) Cracking at Increasing Levels of ϵ_{hoop} . [1]

Examination of the ES specimens under SEM revealed far fewer surface irregularities (transverse grinding striations and pits). Similar to the E specimens, axial cracks perpendicular to the hoop direction were also found along the entire circumference of each specimen. Although thin

cracks branching off of larger cracks (Fig. 4.5d) were observed in some cases, these secondary cracks did not alter the overall pathway of the long axial cracks, consistent with the E specimens. SEM imaging of ES01, which was tested to the onset of acoustic activity, revealed axial cracks around the full circumference of its surface, indicating that crack initiation happens rapidly across the whole specimen surface. Further imaging of the other ES specimens revealed similar axial cracks running across the circumference of each specimen, all parallel to one another. Based on our extensive SEM imaging of these expanding plug specimens, these axial cracks were the only possible source of acoustic activity for the E and ES specimens. Once the expanding plug specimens were loaded past $\sim 0.4\%$ ϵ_{hoop} (the onset of acoustic activity), axial cracks uniformly distributed around the specimens are formed. Any acoustic activity past this critical strain threshold is indicative of the initiation of secondary cracks and widening of pre-existing cracks. The lack of cracks in the transverse direction for both E and ES specimens indicates that the hoop stresses applied during loading were the main drivers for coating cracking.

Mechanical testing and finite element simulations on Cr-coated Zr-alloy tubes by other researchers report higher critical strains correlated to the onset of coating cracking [6-8]; however, several critical variations between these prior studies and the expanding plug testing presented here must be noted. First, the prior works have frequently relied upon transducers to measure strain; these instruments provided only point measurements of strain based on physical contact with the deforming specimen. As a result, such local measurements tend to record the maximum deflection only and overestimate strain. In contrast, DIC techniques provide full-field strain measurements, allowing us to visualize the deformation spectrum of the specimen. Second, these prior studies examined specimens prepared with different coating application methods (3D laser coating, cold-spray, *etc.*) and different coating thicknesses. These variations will generate different

residual stress states within the as-deposited coating and contribute to different stress states at the onset of cracking. Lastly, these studies also have examined a wide range of loading modes, including expanding plug, ring tension, and ring compression [6,8], so the strain at crack onset may exhibit loading mode dependence. This potential loading mode dependence needs to be explored further.

Cross-sectioned expanding plug specimens were also examined under SEM. In general, it was observed that once cracks initiated, they extended through the entire thickness of the coating to the substrate, where propagation was either arrested (Figure 4.5) or much more rarely, laterally deflected. The presence of through thickness cracks in specimens loaded to the onset of acoustic activity further supports this mechanism. Loading of the specimens beyond the critical onset strain ($\sim 0.4\% \epsilon_{hoop}$) seemed to only result in widening of the axial cracks. SEM imaging showed that cracks did not always follow a straight path through the entire coating thickness; this finding stands in sharp contrast with the highly regular, even spacing of axial cracks as observed from the surface. Indeed, we suspect that within the coating thickness, microstructural features may affect the path of the crack. Crack branching and bridging were seen in multiple specimens, where cracks may have grown from pores within the coating (Fig. 4.5e). These observations suggest *coating defects do indeed influence crack penetration radially through the coating thickness but have less of an effect on the axial propagation of the cracks*. At no point during mechanical testing or post-test characterization was the coating observed to delaminate from the substrate but rather remained fully adherent, despite the formation and growth of cracks.

4.2.2 Four-point Bending

After four-point bend testing, all the coated specimens were imaged under the SEM. There was no evidence of coating damage found for B01 and B02, despite the detected acoustic signals

during these tests. It was suspected that the unloading of B01 and B02 may have closed any cracks that formed during testing. Several grinding marks, characteristic of the surface finish, were observed running along the transverse direction (Figure 4.6a) on the surface of each coated specimen (Figure 4.6b). Two modes of damage were primarily seen for B03: thin cracking and striation openings. Thin cracks running parallel to the transverse grinding striations were observed (Figure 4.6c), while 20-25 microns striation openings were often detected in regions that exhibited the highest amounts of tensile strain (Figure 4.6d). These two damage modes could have both possibly contributed uniquely to the detected AE signals. Widening of the grinding striations was found to likely contribute to coating damage, hinting that the surface finish of the coating may be a factor when grinding striations are pulled open in tension.

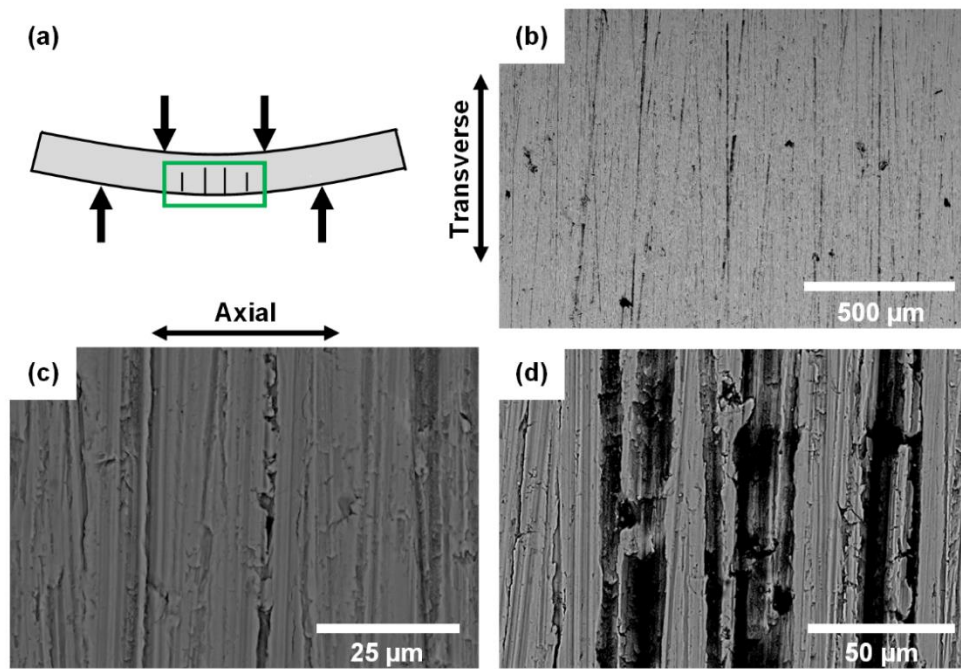


Figure 4.6: Representative SEM Images for Bending Specimen B03: (a) a Schematic of the Loading/Cracking Conditions and the Sample Orientation for SEM Imaging, (b) Several Visible Grinding Marks, (c) Thin Cracking in the Transverse Direction, and (d) Opening of the Striations. [1]

4.3 Summary

This chapter presented the failure mechanisms of room temperature expanding plug and four-point bend samples. The onset of coating cracking was correlated to 0.4 % ϵ_{HOOP} for the expanding plug samples and to 0.4 % ϵ_{XX} for the bending samples. In the expanding plug specimens, axial cracks were found running along the full circumference of each sample, with the widest cracks along the center of the specimen, where the hoop strain concentration was greatest. Through-thickness cracking was determined to occur quickly once cracking was initiated. It was determined that coating defects influence crack penetration radially through the coating thickness but have less of an effect on the axial propagation of the cracks under the expanding plug loading mode. In the bending specimens, thin cracking running parallel to the transverse grinding striations were observed. Widening of these striations was observed with continued deformation, which hints at surface finishing playing a role of coating damage when the striations are pulled open in tension.

Understanding the cracking behavior of coated fuel claddings will inform future design of coated fuel rods. Observing the potential effect of coating defects in the expanding plug loading mode warrants further study into the exact role defects play, in regards to cracking behavior. Generally, axial crack widening was observed with increased deformation in the expanding plug specimens. Although cracking was observed at 0.4 % strain, the integrity of the cracked coating needed to be assessed. Steam oxidation tests conducted on these cracked expanding specimens was conducted in [1], showcasing the effectiveness of the coating to prevent oxidation, even in the presence of cracks. Future studies should investigate if there are critical crack dimensions and strain thresholds that can lead to the ingress of oxygen through the cracks during steam oxidation testing. As pointed out before, future studies should also investigate the role different

coating application processes (i.e. cold-spray vs. 3D laser) play on the overall cracking mechanisms at play and examine why these different processes may exhibit different cracking behaviors at different strain thresholds.

References

- [1] D. C. Roache, A. Jarama, C. H. Bumgardner, F. M. Heim, J. Walters, J. Romero, B. Maier, and X. Li, “Unveiling damage mechanisms of chromium-coated zirconium-based fuel claddings by coupling digital image correlation and acoustic emission,” *Materials Science and Engineering: A*, vol. 774, no. 13, Feb. 2020.
- [2] L. Yang, T. Yang, Y. Zhou, Y. Wei, R. Wu, and N. Wang, “Acoustic emission monitoring and damage mode discrimination of APS thermal barrier coatings under high temperature CMAS corrosion,” *Surface and Coatings Technology*, vol. 304, pp. 272–282, Oct. 2016.
- [3] E. Munch, L. Duisabeau, M. Fregonese, and L. Forunier, “Acoustic Emission Detection of Environmentally Assisted Cracking In Zircaloy-4 Alloy,” 2004. [Online]. Available: https://inis.iaea.org/collection/NCLCollectionStore/_Public/36/105/36105030.pdf.
- [4] T. Nozawa, K. Ozawa, and H. Tanigawa, “Re-defining failure envelopes for silicon carbide composites based on damage process analysis by acoustic emission,” *Fusion Engineering and Design*, vol. 88, no. 9-10, pp. 2543–2546, Oct. 2013.
- [5] S.-K. Kim, J.-G. Bang, D.-H. Kim, I.-S. Lim, Y.-S. Yang, K.-W. Song, and D.-S. Kim, “Hoop strength and ductility evaluation of irradiated fuel cladding,” *Nuclear Engineering and Design*, vol. 239, no. 2, pp. 254–260, Feb. 2009.
- [6] H.G. Kim, I.-H. Kim, Y.-I. Jung, D.-J. Park, J.-Y. Park, and Y.-H. Koo, “Adhesion property and high-temperature oxidation behavior of Cr-coated Zircaloy-4 cladding tube prepared by 3D laser coating,” *Journal of Nuclear Materials*, vol. 465, pp. 531–539, Oct. 2015.
- [7] H. Jiang and J.-A. J. Wang, “Methodology for mechanical property testing of fuel cladding using an expanding plug wedge test,” *Journal of Nuclear Materials*, vol. 446, no. 1-3, pp. 27–37, Mar. 2014.
- [8] Y. Wang, H. Tang, X. Han, W. Feng, X. Zhou, S. Peng, and H. Zhang, “Oxidation resistance improvement of Zr-4 alloy in 1000 °C steam environment using ZrO₂/FeCrAl bilayer coating,” *Surface and Coatings Technology*, vol. 349, pp. 807–815, Sep. 2018.

Chapter 5: Failure Mechanisms at High Temperature (315 °C)

This chapter presents initial findings from the high temperature (315 °C) expanding plug mechanical testing conducted on the chromium-coated fuel cladding samples. Hoop strain and acoustic data are presented for each sample, in addition to limited SEM images of coating cracking from a select sample. The purpose of this chapter is to demonstrate the capability of this novel, high-temperature setup to replicate the expanding plug mechanical testing presented in Chapter 4 at elevated temperatures, in order to characterize the effects of temperature on cracking behavior of the coating. Limited SEM images are provided in this chapter, and from these images, some initial observations about the cracking behavior at temperature may be drawn. Once additional SEM imaging on the remaining high temperature samples is conducted in the near future, a more comprehensive description of the high temperature cracking mechanisms may be proposed. The author notes that the data and initial observations stated in this chapter require further analysis and imaging before any final conclusions may be drawn about the cracking behavior of these samples at elevated temperatures. The author notes that some of the language used in this chapter is adapted from the language used in Chapter 4.

5.1 High Temperature Expanding Plug Testing

3D-DIC and AE were coupled to capture coating crack progression during expanding plug tests at 315 °C, the operating temperature of a typical nuclear reactor. 3D-DIC was used to generate global strain maps of each specimen during loading, and the recorded peak strains for each specimen are listed in Table 5.1. One uncoated and five coated high temperature expanding plug tests were conducted. The uncoated high temperature sample is given the ‘UHE’ ID designation, and the coated high temperature samples are given the ‘HE’ ID designation. The ‘HE’ samples have a similar finish as the ‘ES’ samples tested in Chapter 4 and have a coating thickness of 27

μm . It is important to note that the strains reported in Table 5.1 are the hoop strains associated with mechanical loading only. The thermal strains contributing to the overall stress state of the high temperature samples investigated here are not directly addressed in this work but will be addressed in future work by the author and his colleagues in the near future.

AE detection, on the other hand, was used to establish a baseline comparison between the uncoated and coated samples, such that any acoustic signal above this baseline was assumed to be indicative of coating cracking. Areas with the highest strain concentrations were targeted with subsequent SEM imaging, since these areas were likely the sites of crack initiation. An elevated baseline in the acoustic amplitude was observed, as compared to the room temperature baseline, due to the furnace. The resolution of the acoustic energy data should remain unchanged, because acoustic energy is a measure of peak amplitude and duration of that acoustic event with respect to the baseline acoustic activity recorded. Combining DIC measurements and AE monitoring allowed, to an extent, key coating cracking events to be correlated with DIC deformation measurements.

Table 5.1: Coating Thickness and Max Hoop Strain of High Temperature Expanding Plug Specimens

Test Type	Specimen ID	Average Coating Thickness (μm)	Max ϵ_{hoop} (%)
Expanding Plug	UHE01	0	6.7
	HE01	27	0.30
	HE02	27	1.62
	HE03	27	4.34
	HE04	27	7.07
	HE05	27	7.93

Graphical results presented for each high temperature expanding plug specimen include both stress and normalized cumulative acoustic energy plotted against ϵ_{hoop} for each test (Figure 5.1). The specimens are numbered in ascending order based on the maximum recorded strain.

One uncoated Zr-alloy expanding plug sample was first tested to establish a baseline acoustic signal unassociated with coating cracking. The uncoated sample was loaded beyond yielding and achieved maximum ϵ_{hoop} greater than 6 %. No significant acoustic energy events were detected during testing of the uncoated expanding plug specimens, indicating that acoustic energy signals detected during testing of coated specimens were attributed to the degradation of the coating itself, rather than being associated with damage to the cladding or with excessive background noise from the furnace.

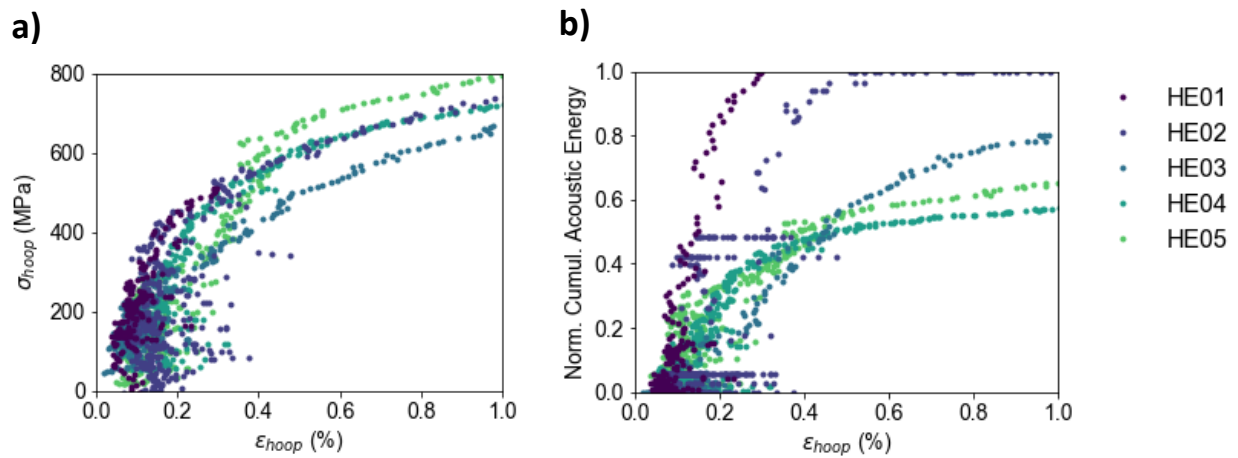


Figure 5.1: a) σ_{hoop} vs. ϵ_{hoop} for HE Specimens and b) Normalized Cumulative Acoustic Energy vs. ϵ_{hoop} for HE Specimens.

Each of the five high temperature coated cladding specimens were tested to varying loads; the load was subsequently correlated to the DIC-measured hoop strain to assess coating cracking onset and degradation with increasing deformation of the specimen. For the ‘HE’ specimens, maximum ϵ_{hoop} ranged from 0.30 % to 7.07 %, and the maximum applied load ranged from around 5000 N to 8500 N. It is clear from Figure 5.1 that distortion in the DIC strain data is prevalent for ϵ_{hoop} below ~0.4 %, even after applying a moving average filter to the DIC images. As determined from DIC images taken prior to loading, the heat distortion in the strain data is ~0.05 %. This distortion in the strain data is apparent at low strains below ~0.4 %, and this complicates the

correlation of acoustic data and hoop stress with hoop strain at low strains. However, past 0.4 %, the noise in the data clears up, and initial observations can be still drawn from this data. One of the major implications of this is the inability to correlate a critical strain threshold (due to mechanical loading) to the onset of cracking at high temperature. This challenge is encountered with the convective air currents from the furnace and will likely be aggravated at higher temperatures. Further studies should examine different ways to reduce the distortion in the data, especially at low strains, for optical techniques like DIC. The link between deformation and coating cracking onset is a critical metric that is needed to inform future design of coated cladding material and should be focused on in future work.

After these initial acoustic energy events, many AE events quickly followed, resulting in linear increases in the normalized cumulative acoustic energy measurements for HE03, HE04, and HE05. It is noted that the acoustic sensor was stopped prematurely for HE02, resulting in the flatlining of the acoustic data at $\sim 0.5\% \epsilon_{hoop}$. One can infer that similar linear acoustic behavior would have been observed for HE02, if the AE was not stopped before the end of the test. As with the room temperature samples, the initial sharp rises in AE events can be attributed to crack initiation all around the circumference of the specimen. This observation is affirmed by the DIC profiles (Figure 5.2), in which high strains are concentrated over the entire center band of the specimens. The subsequent decline in the rate of acoustic activity is suspected to be correlated to crack saturation with subsequent acoustic activity indicating crack propagation, rather than crack initiation.

Representative DIC strain maps of HE03, illustrating the progression of deformation are presented in Figure 5.2 below. As loading progressed, the expansion of the plunger resulted in the development of a strain band along the center of the specimen (Figure 5.2d), similar to the room

temperature samples discussed in Chapter 4. Localized strain concentrations picked up by 3D-DIC can be attributed to the aggregate effect of the opening of multiple cracks in that specific region.

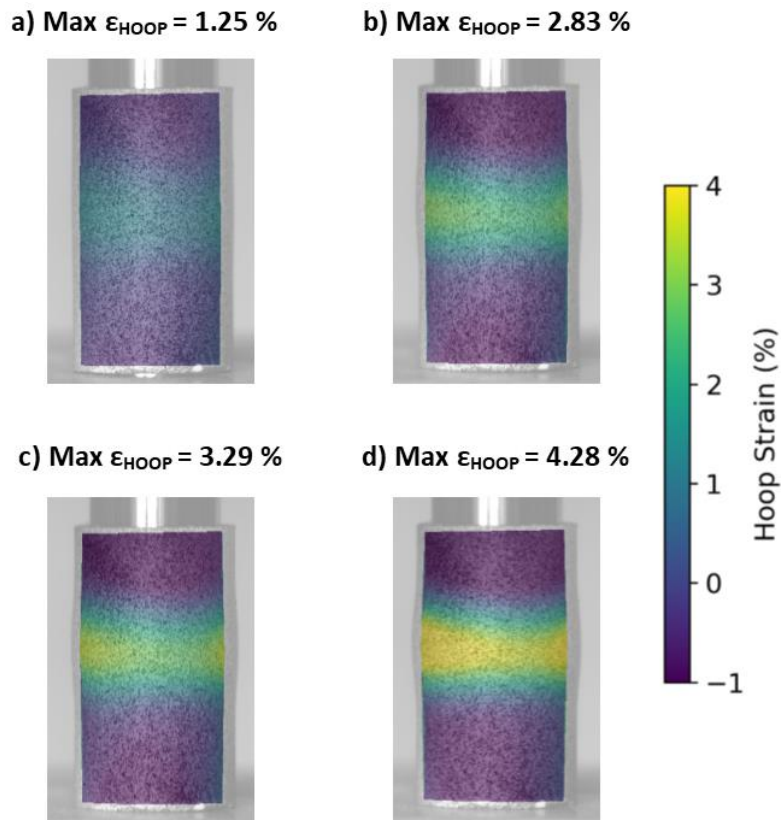


Figure 5.2: Typical Spatial ϵ_{hoop} Progression during an Expanding Plug Test, Here for HE03.

5.2 High Temperature Crack Characterization

Figure 5.3 presents surface and cross-section SEM images of HE05. Figure 5.3a shows the presence of dense, angled (24° to 38° from axial) cracking along the circumference of the specimen. This angled cracking was most notable along the center of the specimen, where deformation was the greatest. As with the room temperature samples, these angled cracks tapered away from the center of the specimen. Sparse, axial cracking was also observed along areas on the surface away from the center of the sample. The uniformity of these angled cracks suggests a mixed mode fracture mechanism of the coating at higher temperatures.

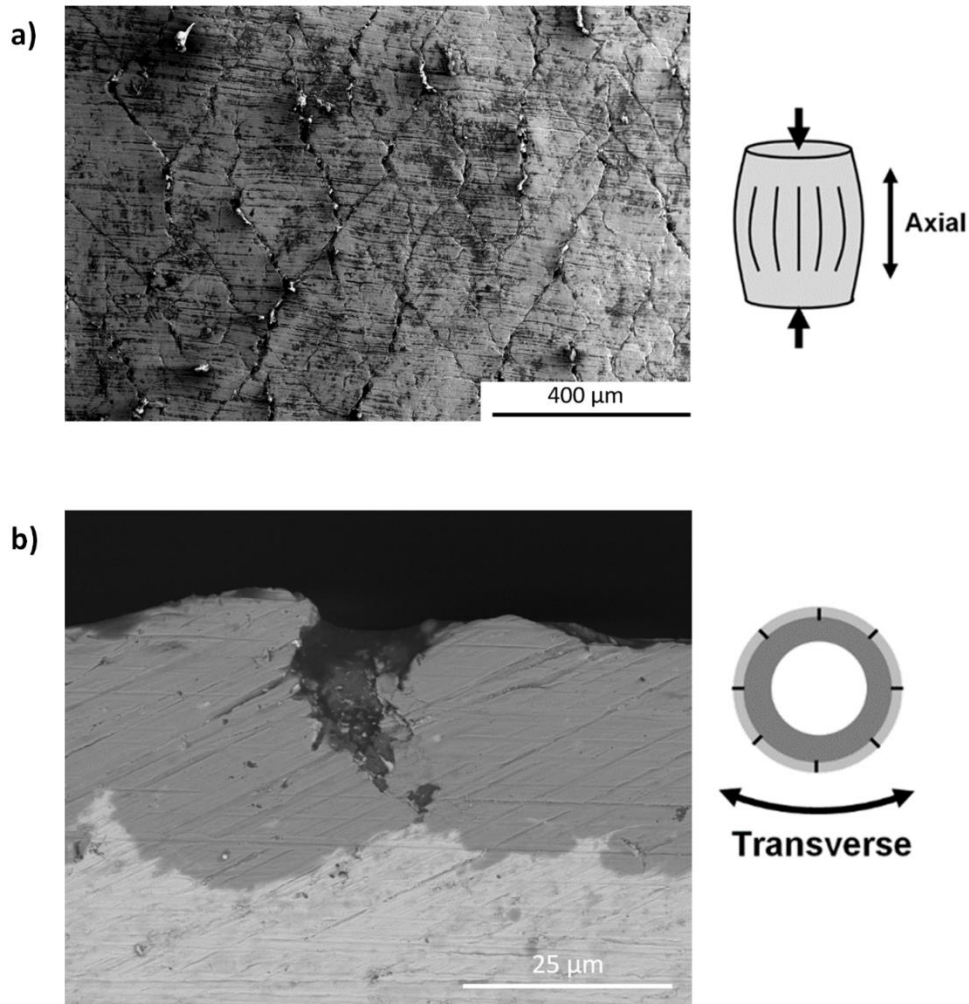


Figure 5.3: SEM Images of HE05: (a) Image of Specimen Surface in Region of Greatest Deformation Showing Angled Cracks, (b) Image of Specimen Cross-Section Showing Through-thickness Cracking.

When the coefficient of thermal expansion (CTE) between a thin or thick film and its substrate differ significantly, adhesion of the coating becomes a key issue at higher temperatures [1]. The difference in the CTE between the coating and substrate is defined by Equation 5.1.

$$\Delta CTE = \frac{\epsilon_{THERMAL}}{\Delta T} \quad (5.1)$$

$\epsilon_{THERMAL}$ denotes the thermal strain, while ΔT denotes the temperature difference. If there is a large mismatch between the two CTEs, then high stresses in the coating may be generated that

can lead to delamination and cracking [1]. Chromium and zircaloy have similar CTEs ($6.2 \mu\text{m}/\text{m}^\circ\text{C}$ for chromium and $6 \mu\text{m}/\text{m}^\circ\text{C}$ for zircaloy) [2,3], suggesting that their differing thermal expansion rates is most likely not the main cause for this unique cracking behavior, but further study is needed to address this possibility. Coating thickness may also play a role in the CTE of the coating and is another variable that warrants further examination in future studies. It has been shown that coatings can be subjected to a number of different failure modes at high temperatures, such as oxidation, corrosion, spallation and fatigue cracking [4]. The cracking behavior of these coated cladding samples at high temperature warrants further study and further imaging to confirm and understand the mechanisms behind this new observed crack pattern.

Figure 5.3b shows a cross-section image of HE05. Similar to the room temperature specimens, through-thickness coating cracks can be observed, and suggests that the cracking behavior through the thickness of the coating remains the same even at elevated temperatures. This observation warrants further study and further imaging to confirm this cracking behavior.

5.3 Summary

This chapter presents the cracking behavior of a single imaged high temperature sample. Five expanding plug specimens were deformed up to ϵ_{HOOP} of 7.93 %. The reported strains in this chapter are due solely to mechanical loading and do not account for the thermal strains exhibited by the samples at elevated temperatures. Due to the significance of the distortion in the DIC images at below $\sim 0.4 \% \epsilon_{\text{HOOP}}$, a critical strain threshold associated with cracking initiation could not be achieved. The most highly deformed specimen was imaged under SEM to reveal a different fracture pattern of the coating, as compared to the room temperature samples. Long axial cracks were observed along the full circumference of the surface in the room temperature cracks; however, angled cracks along the surface of the high temperature cracks were observed.

This new fracture pattern suggests different fracture mechanisms are at play at elevated temperature, and further imaging is needed to verify these initial observations. Like the room temperature samples, through-thickness cracking was observed in the imaged high temperature sample. Table 5.2 provides a comparison of the observed cracking behavior of the room temperature and high temperature samples.

Table 5.2: Comparison of Crack Patterns in Room Temperature and High Temperature Expanding Plug Samples.

Expanding Plug Specimens	Crack Patterns along the Surface	Crack Patterns of Cross-Section
Room Temperature	-Axial cracks running along the full circumference of the sample. -Cracks were widest in the areas corresponding to the highest deformation.	-Through-thickness cracking observed, even at the onset of cracking.
High Temperature	-Angled cracks (24° to 38° from axial) running along the full circumference of the sample. -Cracks were widest in the areas corresponding to the highest deformation.	-Through-thickness cracking observed.

To reiterate, the claims made in this chapter are based on initial observations made from limited SEM images. Further imaging and analysis of the DIC are required to verify the initial observations stated in this chapter and to draw robust conclusions.

References

- [1] R. K. Singh, D. R. Gilbert, J. Fitz-Gerald, S. Harkness, and D. G. Lee, “Engineered Interfaces for Adherent Diamond Coatings on Large Thermal-Expansion Coefficient Mismatched Substrates,” *Science*, vol. 272, no. 5260, pp. 396–398, Apr. 1996.
- [2] “Chromium (Cr) - Properties, Applications,” 15-Jul-2013. [Online]. Available: <https://www.azom.com/article.aspx?ArticleID=9081>.
- [3] “Zircaloy-4 (Alloy Zr4) (UNS R60804),” 11-Jun-2013. [Online]. Available: <https://www.azom.com/article.aspx?ArticleID=7644>.
- [4] *Coatings for high-temperature structural materials: trends and opportunities*. Washington, D.C.: National Academy Press, 1996.

Chapter 6: Conclusions and Future Work

In this work, four-point bend testing at room temperature and expanding plug testing at room temperature and at 315 °C were performed on chromium-coated Zr-alloy claddings. In situ 3D-DIC and AE monitoring were coupled to directly correlate spatial strain maps with acoustic energy evolution to study coating degradation during loading. Mechanical testing of uncoated specimens and SEM imaging confirmed that acoustic activity detected during loading of coated specimens is indicative of coating damage. Subsequent SEM imaging was conducted to characterize cracking of the coating and to observe the fracture mechanisms of the coating at various strains. The author notes that parts of this chapter are adapted from adapted from the author's peer reviewed journal article titled "Unveiling Damage Mechanisms of Chromium-Coated Zirconium-Based Fuel Claddings by Coupling Digital Image Correlation and Acoustic Emission" published in *Materials Science and Engineering: A* [1].

During the room temperature expanding plug tests, cracks formed axially around the circumference of the specimens, initiating at $\sim 0.40\% \epsilon_{\text{HOOP}}$; this result was consistent for both E and ES specimens. For four-point bending tests, grinding striations characteristic of the coating surface were found to likely widen and contribute to coating damage, beginning at $\sim 0.40\% \epsilon_{\text{XX}}$. SEM imaging of the expanding plug specimens revealed regularly spaced axial cracking around the full circumference of the specimens, which penetrated through the entire thickness of the coating. It is suspected that the crack widening and axial propagation, which were seen to be consistent across the circumference, are primarily driven by the loading mode, whereas the microstructure of the coating and defects on the surface of/within the coating are responsible for the through thickness path of the cracks, as well as crack deflection, bridging, etc. observed in some of the SEM images. For four-point bending specimens, the presence of transverse grinding

striations parallel to the direction of cracking, as well as possible crack closing due to specimen unloading, made it difficult to properly evaluate initial crack formation.

A novel, high temperature expanding plug mechanical testing setup was also presented in this work to study failure mechanisms of coated fuel claddings at elevated temperatures.

Applying a moving average filter to the DIC images prior to processing accounted for heat distortion prevalent during high temperature studies, but that distortion was significant at ϵ_{HOOP} below $\sim 0.4\%$. The strains reported for the high temperature samples are indicative of strains associated with mechanical loading and do not account for any thermal strains the samples experience at high temperature. During the high temperature expanding plug tests, angled cracking was observed across the circumference of a select sample. This fracture pattern differs from the fracture pattern observed in the room temperature specimens and suggest different fracture mechanisms are at play at $315\text{ }^{\circ}\text{C}$. As with the room temperature samples, through-thickness cracking was observed in cross-section SEM images of a select high temperature sample. Limited SEM imaging of the high temperature samples was conducted. The author notes that the initial observations made about the high temperature samples need further analysis and imaging, before any robust conclusions can be drawn.

The work presented here offers insight into the key cracking mechanisms at play in chromium-coated Zr-alloy based fuel claddings. Understanding the cracking behavior of coated claddings is critical in their implementation in nuclear reactors, because cracking can lead to the ingress of oxygen, which is a major concern during beyond design-basis accident conditions. This work provides critical observations of the cracking behavior of room temperature samples, and future studies should examine if there are critical crack dimensions and corresponding strain thresholds that can lead to the ingress of oxygen during steam oxidation testing. Further

studies should also investigate the role different coating application processes play on the overall cracking mechanisms and should also aim to understand why these different processes may exhibit different cracking behaviors at different strain thresholds.

With the proposed high temperature setup, further mechanical testing should be conducted to determine how cracking mechanisms of chromium coatings change with different temperatures. In particular, thermal mismatch caused by differing coefficients of thermal expansion from the chromium coating and the zirconium-based substrate should be investigated more in-depth. Accident condition mechanical testing at 1200 °C can provide key insight into relevant coating cracking during nuclear meltdowns and can inform future design and implementation of coated nuclear fuel claddings. At such high temperatures, oxidation of the cladding may arise, and its effects on the integrity of the coating and on mechanical performance should be investigated. The effectiveness of the coating is comprised with the ingress of oxygen through cracks during beyond design-basis accident conditions, and thus the findings presented in thesis regarding cracking behavior is timely. Determining critical strain thresholds associated with key crack behaviors should be at the forefront of similar future mechanical testing at higher temperatures.

In order to curb global carbon emissions to address the immediate issue of climate change, nuclear energy needs to be a critical component of the global energy grid. After nuclear accidents such as Fukushima in Japan, there is an increased amount of negative public perception around nuclear energy. Even though nuclear energy results in fewer deaths than other energy sources, such as fossil fuels, the nuclear energy community has a responsibility to lower the stigma surrounding nuclear energy, namely by improving the reliability and durability of nuclear reactor components to prevent future nuclear accidents. This work is directly relevant to the fuel

claddings used in a number of nuclear reactors around the world, and it is the author's hope that this work helps improve public perception around nuclear energy.

References

- [1] D. C. Roache, A. Jarama, C. H. Bumgardner, F. M. Heim, J. Walters, J. Romero, B. Maier, and X. Li, “Unveiling damage mechanisms of chromium-coated zirconium-based fuel claddings by coupling digital image correlation and acoustic emission,” *Materials Science and Engineering: A*, vol. 774, no. 13, Feb. 2020.